



# Global monthly ocean dissolved oxygen (1960–2023) reconstructed to 5902 m with BLENDR, a Bayesian-optimized ensemble learning framework

Mingyu Han<sup>1</sup>, Xiaogang Xing<sup>2</sup>, and Yuntao Zhou<sup>1</sup>

<sup>1</sup>State Key Laboratory of Submarine Geoscience and School of Oceanography,  
Shanghai Jiao Tong University, Shanghai, China

<sup>2</sup>State Key Laboratory of Satellite Ocean Environment Dynamics (SOED), Second Institute of Oceanography,  
Ministry of Natural Resources, Hangzhou, China

**Correspondence:** Yuntao Zhou (ytzhou@sjtu.edu.cn)

Received: 14 December 2025 – Discussion started: 28 December 2025  
Revised: 27 April 2026 – Accepted: 25 May 2026 – Published: 3 June 2026

**Abstract.** Oceanic oxygen levels, crucial for marine ecosystems and biogeochemical cycles, have declined significantly over the past few decades due to climate change, posing severe environmental risks. However, historical dissolved oxygen (DO) measurements, especially below 2000 m, remain sparse, limiting comprehensive annual and seasonal analyses. Here, we introduce the BLENDR framework (Bayesian-optimized Learning and ENsemble modeling for Data Reconstruction), a Bayesian-optimized ensemble of six machine-learning models (Random Forest, XGBoost, LightGBM, CatBoost, Extremely Randomized Trees and Histogram-based Gradient Boosting) fused via a spatially coherent dynamic weighting scheme, to reconstruct global monthly DO distributions at a  $1^\circ \times 1^\circ$  resolution from the surface to 5902 m from 1960 to 2023. Validation against an independent dataset demonstrated that BLENDR achieves better performance than any individual model, with an  $R^2$  of 0.968. Our dataset captures depth-dependent deoxygenation, with the most pronounced decline occurring between 150 and 200 m at approximately  $-0.12 \mu\text{mol kg}^{-1} \text{yr}^{-1}$ , and shows severely accelerated oxygen loss in the Arctic Ocean and North Atlantic over the past decade. This work provides a long-term, global monthly DO product from the ocean surface to 5902 m. The bathypelagic DO data provided in this work are a significant contribution to deep ocean oxygen dynamics and global biogeochemical cycles. The data product is publicly accessible at <https://doi.org/10.5281/zenodo.19705526> (Han and Zhou, 2026).

## 1 Introduction

Over the past few decades, dissolved oxygen (DO) levels in open oceans have been rapidly decreasing (Breitburg et al., 2018; Keeling et al., 2010), primarily driven by climate change (Deutsch et al., 2011). This continuous decline has severely affected marine organisms and ocean chemistry, disrupting marine productivity, and biodiversity (Gruber, 2011; Stramma et al., 2012). Climate models predict that global warming will further accelerate this deoxygenation (Oschlies et al., 2018), potentially adversely affecting aerobic marine organisms within this century (Sampaio et al., 2021) and altering biogeochemical cycles (Gruber, 2004; Berman-Frank

et al., 2008). Therefore, it is important to develop a comprehensive, high-resolution reconstruction of ocean DO across both space and depth to accurately quantify historical deoxygenation trends, identify regional hotspots, and inform future ecosystem and climate projections.

Despite significant progress in oceanographic data collection, severe gaps in historical DO data persist, hindering comprehensive analysis. For instance, the World Ocean Database (WOD) (Mishonov et al., 2024) compiles DO profiles from research cruises and floats, yet observations remain sparse and unevenly distributed across much of the global ocean. This sparse spatial coverage severely limits the use of data imputation methods to reconstruct four-dimensional DO

fields. Furthermore, although many Earth System Models (ESMs) attempt to simulate global oceanic DO, these models are not directly constrained by historical DO observations in the way observation-based reconstructions are, leading to error propagation (Pathak et al., 2023). Thus, numerical models diverge significantly from in situ observations and underestimate actual DO decline trends (Bopp et al., 2013; Cocco et al., 2013; Long et al., 2016; Kwiatkowski et al., 2020), which reduces confidence in model-based assessments of ocean deoxygenation, Oxygen Minimum Zones (OMZ), and biogeochemical cycles.

Classical interpolation methods have long been employed to map oceanic DO. Zhou et al. (2022) combined geostatistical regression with Monte Carlo methods to estimate changes in the area of OMZs globally and regionally from 1960 to 2019. Garcia et al. (2024) applied objective analysis in the World Ocean Atlas 2023 (WOA23) to produce internally consistent annual and monthly DO fields from 1965 to 2022. Gouretski et al. (2024) developed an automated quality control procedure to detect outliers and correct biases in ocean oxygen profiles, producing a consistent global dataset from 1920 to 2023. Roach and Bindoff (2023) used Data Interpolating Variational Analysis (DIVA) to generate a global high-resolution oxygen atlas from 1955 to 2018.

Recently, machine learning approaches have been increasingly adopted in Earth system science and oceanography because they can efficiently exploit large datasets and capture complex nonlinear relationships (Reichstein et al., 2019; Shen, 2018). Giglio et al. (2018) utilized a random forest regression model to estimate the oxygen concentration at 150 m in the Southern Ocean on the basis of Argo data from 2008 to 2012. Sharp et al. (2023) reconstructed a global DO dataset called GOBAI-O<sub>2</sub> using feedforward neural networks and random forest regression, spanning the years 2004–2022 with a monthly resolution and extending from the ocean surface to a depth of 2000 m. Ito et al. (2024) developed a machine-learning ensemble of neural networks and random forests trained on historical shipboard and biogeochemical Argo DO profiles to generate gridded monthly oxygen fields. Crucially, most existing machine-learning reconstructions are limited to the upper 2000 m of the water column, leaving the vast bathypelagic zone (below 2000 m) poorly constrained, despite its importance for global carbon storage and long-term oxygen budgets. While some of the DO data reconstruction studies focus on specific regions (Giglio et al., 2018; Huang et al., 2023), some span longer time spans (Roach and Bindoff, 2023; Ito et al., 2024), and some achieve higher temporal or spatial resolutions (Sharp et al., 2023; Shao et al., 2023), it is challenging to simultaneously address all aspects.

Here, we introduce the BLENDR framework (Bayesian-optimized Learning and ENsemble modeling for Data Reconstruction), which integrates six tree-based learners, Random Forest, XGBoost, LightGBM, CatBoost, Extremely Randomized Trees and Histogram-based Gradient Boost-

ing, each tuned via Bayesian hyperparameter optimization. Model outputs are fused with a spatially coherent dynamic weighting scheme that combines global prior model skill with locally constrained error information. BLENDR produces a global 1° × 1° monthly DO dataset from 1960 to 2023 down to 5902 m, filling critical deep-ocean gaps. We evaluated the ensemble using 8-fold temporal cross-validation and an independent filtered subset of the Global Ocean Data Analysis Project v2.2023 (GLODAPv2) (Olsen et al., 2016) after all the profiles that overlap with the WOD (CTD and OSD) collections were removed to ensure independence. We also quantified the measurement, grid and algorithm uncertainties. Using this product, we analyzed global, basin-scale and depth-resolved DO distributions and long-term deoxygenation trends, including the vertical structure and multi-basin evolution of OMZ extent, changes in basin-scale oxygen content and their recent acceleration, and hemispheric differences in DO seasonality. In addition, we quantified the influence of a recently documented systematic bias in delayed-mode Argo DO by comparing reconstructions with and without a uniform correction applied to Argo profiles. To capture regional differences in oxygen storage and trends, we divided the global ocean into ten basins: the North Pacific (NP), Equatorial Pacific (EP), South Pacific (SP), North Atlantic (NA), Equatorial Atlantic (EA), South Atlantic (SA), North Indian (NI), South Indian (SI), Southern Ocean (SO) and Arctic Ocean (AO). The basin boundaries (Fig. 6a) follow Schmidtko et al. (2017).

## 2 Data and methods

### 2.1 Data

#### 2.1.1 Observational data of dissolved oxygen

We assembled our observational DO database by merging quality-controlled profiles from the Array for Real-Time Geostrophic Oceanography dataset (Argo, <https://argo.ucsd.edu>, last access: 5 March 2025) (Wong et al., 2020) with Conductivity-Temperature-Depth (CTD) and Ocean Station Data (OSD) measurements archived in the World Ocean Database 2023 (WOD, <https://www.ncei.noaa.gov/products/world-ocean-database>, last access: 5 March 2025) (Mishonov et al., 2024). Each profile consists of oxygen concentrations measured at multiple depths at a given date and location. For Argo, we restricted the data to post-processed delayed-mode profiles and retained only records flagged as good. Overlapping profiles were deduplicated by keeping the version with finer vertical sampling. Although we initially followed Schmidtko et al. (2017) in treating the combined dataset as free of systematic errors, recent evidence indicates a systematic offset between Argo and CTD/OSD. Accordingly, following Wang et al. (2025), we applied a uniform +1.69 μmol kg<sup>-1</sup> bias correction to all delayed-mode Argo DO profiles. Annual profile counts of OSD, CTD, and Argo

observations are shown in Fig. S1 in the Supplement. Although DO observations below 2000 m become sparser with depth, they remain available across most basins (Table S1).

To obtain an independent evaluation set, we constructed a validation subset from GLODAPv2 (Olsen et al., 2016) after removing any profiles that overlap with our training pool from CTD and OSD. We compared the two collections profile by profile and applied a conservative space and time filter: for each oxygen profile in GLODAPv2, we searched the CTD and OSD records for profiles within  $\pm 1^\circ$  in longitude,  $\pm 1^\circ$  in latitude, and the same calendar month and year. When such a match existed, we treated the pair as duplicates and excluded the GLODAPv2 profile from validation. This reduced the original 56 480 GLODAPv2 profiles to 8020. The spatial distribution and temporal histograms of the filtered GLODAPv2 dataset are shown in Fig. S2. A manual spot check confirmed that no additional space-time matches remained. We therefore use this filtered GLODAPv2 dataset as an independent benchmark for assessing our reconstruction.

### 2.1.2 Reanalysis data of environmental factors

We obtained monthly ocean temperature ( $T$ ,  $^\circ\text{C}$ ), salinity ( $S$ , PSU), meridional velocity and zonal velocity (MV and ZV,  $\text{m s}^{-1}$ ) from the Ocean Reanalysis System 5 (ORAS5) gridded ocean dataset with a spatial resolution of  $0.25^\circ \times 0.25^\circ$  and 75 vertical levels (Table S2), ranging from the ocean surface to 5902 m in depth (<https://cds.climate.copernicus.eu/datasets/reanalysis-oras5>, last access: 5 March 2025).

## 2.2 BLENDR framework

We developed the BLENDR framework to reconstruct a global, monthly DO product from 1960 through 2023. The process began by assembling and preprocessing all available in situ DO profiles together with key environmental factors ( $T$ ,  $S$ , and currents) onto a monthly  $1^\circ \times 1^\circ$  grid with 75 vertical levels. Next, each of the six tree-based learners (Random Forest, XGBoost, LightGBM, CatBoost, Extremely Randomized Trees and Histogram-based Gradient Boosting) underwent Bayesian hyperparameter tuning via Optuna's Tree-structured Parzen Estimator (TPE) sampler, ensuring that each model minimized the cross-validation RMSE (Akiba et al., 2019). Once optimized, the models were trained on the full gridded dataset and predicted the DO concentration at every valid grid cell, producing six complete four-dimensional DO fields. These outputs were then merged through a spatially coherent dynamic weighting scheme (Dietterich, 2000). This approach assigns prior weights based on each model's temporal cross-validation skill, derives locally varying weights from model agreement with available observations, and then propagates these local weights to neighboring grid cells through Gaussian kernel smoothing while gradually shrinking them toward the prior weights as observational support decreases. The resulting ensemble therefore

adapts continuously in space while retaining stable behavior in poorly observed regions. Finally, model performance was assessed using 8-fold temporal cross-validation and an independent evaluation against the filtered GLODAPv2 dataset (Olsen et al., 2016). The overall workflow of the BLENDR framework is shown in Fig. 1.

### 2.2.1 Data processing

In this study, all ocean DO observation data included temporal and spatial information, such as year, month, day, longitude, latitude, and measurement depth. The longitude and month are both periodic features. For instance, longitude ranges from 0 to  $360^\circ$ , with  $360^\circ$  overlapping with  $0^\circ$ , and month represents an annual cycle that repeats every 12 months. To address this issue, we followed the approach of Gade (2010) and Tang et al. (2019) by representing longitude and month using sine and cosine functions.

Although ORAS5 is provided on a  $0.25^\circ \times 0.25^\circ$  grid, we upscaled it by simple averaging to a common  $1^\circ \times 1^\circ$  grid with 75 depth levels. For each  $1^\circ$  grid cell, we averaged all available ORAS5 values located within that cell. DO observations were binned to each grid cell by averaging all points that fell within the cell at the same month and depth level. To address potential multicollinearity, which can lead to instability in subsequent modeling and increase the risk of overfitting, we analyzed correlations between the 11 factors. No correlation coefficient exceeded 0.5, so variable selection was not necessary in this case (Fig. S3). A complete list of predictors, with abbreviations and data sources, is shown in Table 1.

### 2.2.2 Machine learning models

We used six tree-based algorithms to reconstruct dissolved oxygen. Each model offers a different balance of bias, variance, and computational efficiency. We chose them because of their robust performance in regression tasks and their ability to handle nonlinear relationships. We used six models because they span the main tree learning paradigms, namely, bagging and boosting; thus, their strengths are complementary, and their residual errors are expected to be only weakly correlated. We kept the ensemble within the tree family because dissolved oxygen depends on nonlinear interactions among multiple drivers, and the data contain missing values, conditions under which decision trees perform well without elaborate feature engineering. In our initial model screening under the same input features and validation framework, the tested neural-network models, including a convolutional neural network and a back-propagation neural network, did not show an accuracy advantage over Random Forest, while requiring more tuning effort and providing less interpretability. Therefore, we focused the final ensemble on tree-based learners. All models were trained on the same input features

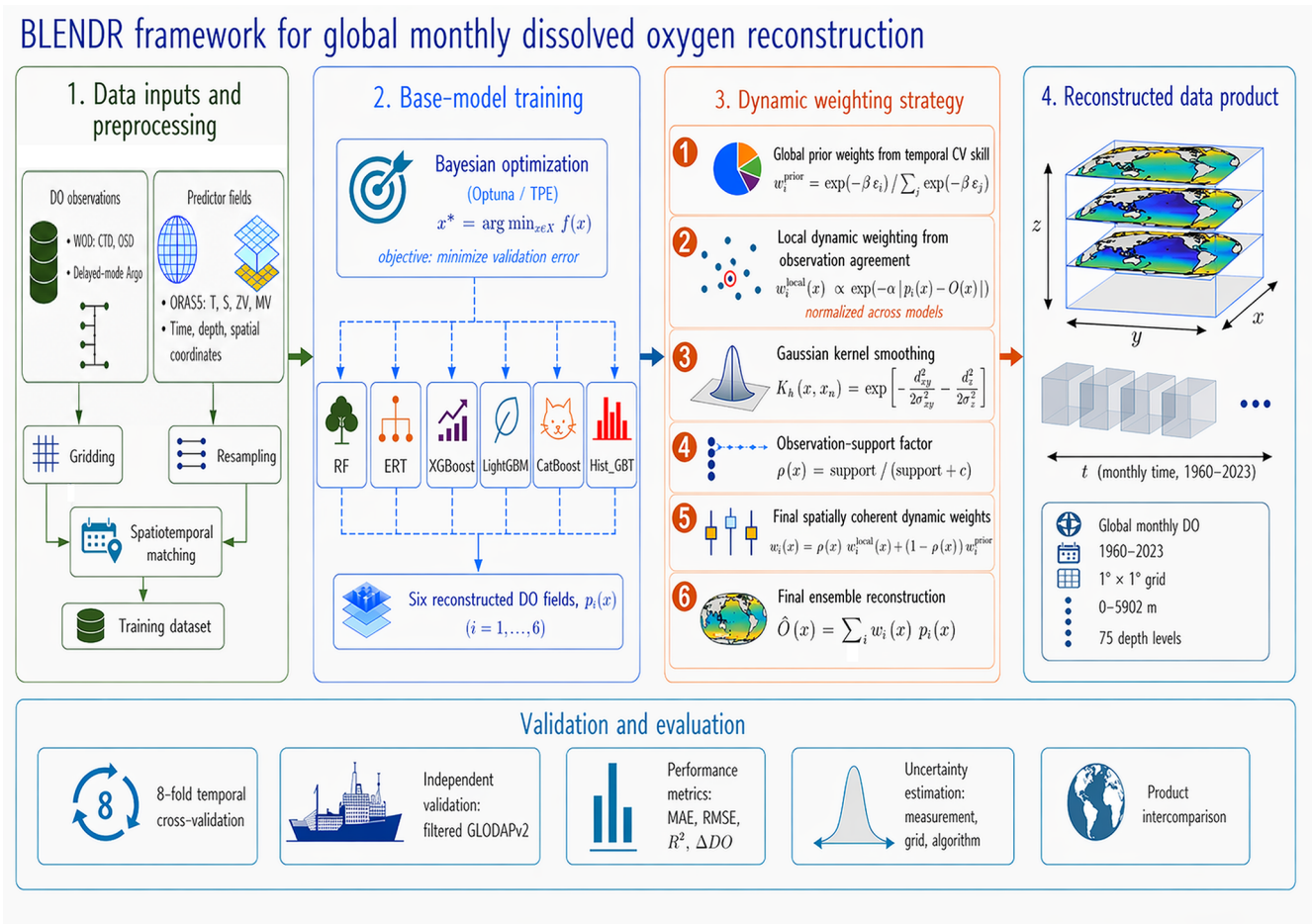


**Figure 1.** Overview of the BLENDR framework.

**Table 1.** Predictors, abbreviations and products/references of the 11 environmental factors.

Predictor	Abbreviation	Product/Reference
$\sin(\text{latitude} \cdot \pi / 180)$	coord_1	WOD (CTD + OSD) & Argo
$\sin(\text{longitude} \cdot \pi / 180) \cdot \cos(\text{latitude} \cdot \pi / 180)$	coord_2	
$-\cos(\text{longitude} \cdot \pi / 180) \cdot \cos(\text{latitude} \cdot \pi / 180)$	coord_3	
Year	Year	ORAS5
$\cos(\text{month} \cdot 2\pi / 12)$	time_cos	
$\sin(\text{month} \cdot 2\pi / 12)$	time_sin	
Depth	Depth	
Temperature	$T$	ORAS5
Salinity	$S$	
Zonal Velocity	ZV	
Meridional Velocity	MV	

Note: The observational data were from WOD and Argo. The data from ORAS5 were  $0.25^\circ \times 0.25^\circ$  monthly mean profile data.

and tuned via Bayesian optimization (Sect. 2.2.3). Below, we briefly describe each model.

Random Forest (RF) builds many decision trees on bootstrap samples and averages their outputs (Breiman, 2001). It selects a random subset of features at each split. This ran-

domness reduces overfitting. RF handles large datasets well and is robust to outliers. RF represents classical bagging, and Extremely Randomized Trees (ERTs) push this idea toward stronger randomness (Geurts et al., 2006). It selects split thresholds at random rather than searching for the best

cut. It uses the full dataset rather than bootstrapping. This strong randomization further lowers variance at modest cost in terms of bias. CatBoost is a gradient-boosting library designed for categorical features (Prokhorenkova et al., 2018). It uses ordered target statistics to avoid target leakage. It grows symmetric trees and performs efficient leaf pruning. CatBoost often converges faster and requires less tuning of the learning rate. XGBoost implements gradient boosting with second-order optimization (Chen and Guestrin, 2016). It adds regularization to control the complexity of the tree. It uses approximate split finding to speed up training on large data. XGBoost balances accuracy and runtime efficiency. LightGBM uses histogram-based binning and leaf-wise tree growth (Ke et al., 2017). It buckets continuous features into bins, reducing the amount of memory. Trees grow by selecting splits that yield the greatest loss reduction. LightGBM is highly efficient for large feature sets and large datasets. Histogram-based Gradient Boosting (Hist\_GBT) follows Friedman's original gradient boosting framework (Guryanov, 2019; Friedman, 2001). It fits a sequence of weak learners to the negative gradient of the loss. It also uses histogram binning for faster split evaluation. Hist\_GBT offers good accuracy in high-dimensional settings. XGBoost, LightGBM and Hist\_GBT are gradient boosting methods but differ in terms of split criteria and optimization details.

### 2.2.3 Bayesian parameter optimization

To optimize hyperparameters across different machine learning models in a systematic and efficient manner, we employed Bayesian optimization using the Optuna framework (Akiba et al., 2019). Unlike grid or random search, this approach builds a statistical model of how settings affect error and then tests promising regions more often, finding good configurations with fewer trials and providing a fair, comparable procedure across models. Specifically, at each trial, a candidate set of hyperparameters is sampled, the model is trained, and its validation error is recorded. Optuna then uses all the previously tested hyperparameter–error pairs to update the surrogate model and proposes the next set of hyperparameters where the error is expected to decrease.

Bayesian optimization was used to construct a probabilistic surrogate model of the objective function  $f(\mathbf{x})$ , where  $\mathbf{x}$  is a vector of hyperparameters. The optimization seeks to identify the optimal  $\mathbf{x}^*$  that minimizes  $f$ :

$$\mathbf{x}^* = \arg \min_{\mathbf{x} \in \chi} f(\mathbf{x}) \quad (1)$$

Here,  $\chi$  denotes the hyperparameter space. In practice, we used the Tree-structured Parzen Estimator (TPE) sampler in Optuna to approximate the objective function. After each trial, the observed pairs  $(\mathbf{x}, f(\mathbf{x}))$  are divided into a “good” set with low objective values and a “bad” set with high values, using a quantile threshold. The TPE then fits two probability density functions over the hyperparameters, one for the

good set and one for the bad set, and proposes new candidates in regions where the ratio of these densities is large. This strategy is equivalent to selecting the next sampling point to maximize the Expected Improvement (EI):

$$\text{EI}(X) = \int_{-\infty}^{y^*} (y^* - y) \cdot p(y|x) dy \quad (2)$$

where  $y^*$  is the current best objective value. The sampling focuses on regions with high EI. In plain terms, the EI favors trials that are expected to reduce the error relative to the current best, so the search is concentrated on the most promising parts of the space.

To reduce temporal overfitting and preserve model generalizability across decades, hyperparameter optimization was conducted using a subset of data from eight years (1960, 1968, 1976, 1984, 1992, 2000, 2008, 2016). These years were chosen to sample different climate and sampling regimes across the six-decade period, ensuring that the optimized models are robust to temporal shifts in data availability and underlying oceanic conditions. The objective function minimized the Mean Squared Error (MSE) on an independent validation set derived from eight other test years (1967, 1975, 1983, 1991, 1999, 2007, 2015, and 2023). We chose the MSE because it penalizes large errors more heavily, which is desirable when evaluating gridded oxygen where occasional large deviations can dominate downstream diagnostics. The objective function was defined as follows:

$$\text{MSE} = \frac{1}{n} \sum_{i=1}^n (\hat{y}_i - y_i)^2 \quad (3)$$

Each model was optimized over its own hyperparameter space, with the best-performing configuration recorded for final training and subsequent prediction on independent test data. This consistent, data-driven approach ensured fair comparability across all six learners and minimized bias from manual tuning. Below, we summarize the search space and optimal parameters in Table 2.

### 2.2.4 Multi-model fusion and dynamic weighting scheme

We fused the predictions of the six base models into a single reconstruction using a spatially coherent dynamic weighting scheme. The aim was to combine global model skill with local observational constraint while maintaining spatial continuity in the weight field. This formulation is consistent with ensemble weighting based on model skill, locally calibrated weighting informed by nearby observations, and kernel-based estimation for spatially varying relationships (Raftery et al., 2005; Kleiber et al., 2011; Brunson et al., 1996). Each model was first assigned a global prior weight derived from its average predictive skill in temporal cross-validation. These prior weights served as a stable baseline in regions with weak observational support. We then introduced locally varying weights based on the agreement between model predictions and available observations. To avoid

**Table 2.** Hyperparameter search spaces and optimal values.

Model	Hyperparameter	Search Range	Best Value
ERT	n_estimators	50–500	452
	max_depth	3–20	20
	min_samples_split	2–20	15
	min_samples_leaf	1–10	2
	max_features	0.1–1.0	0.577
	bootstrap	{True, False}	False
	CatBoost	iterations	50–1000
depth		3–12	12
learning_rate		0.005–0.3	0.077
l2_leaf_reg		10 <sup>-5</sup> –10	0.009
random_strength		10 <sup>-5</sup> –10	7.053 × 10 <sup>-5</sup>
bagging_temperature		0–1	0.122
border_count		32–255	120
Hist_GBT	learning_rate	0.005–0.3	0.177
	max_iter	50–1000	928
	max_depth	3–12	8
	min_samples_leaf	5–50	41
	l2_regularization	10 <sup>-5</sup> –10	0.932
	max_bins	32–255	251
	LightGBM	n_estimators	50–1000
max_depth		3–12	12
learning_rate		0.005–0.3	0.264
num_leaves		10–300	145
min_child_samples		5–50	18
subsample		0.5–1.0	0.683
colsample_bytree		0.5–1.0	0.828
reg_alpha		10 <sup>-8</sup> –10	6.15 × 10 <sup>-7</sup>
reg_lambda		10 <sup>-8</sup> –10	4.708
RF		num_trees	10–200
	min_leaf_size	10–100	10
XGBoost	n_estimators	50–1000	138
	max_depth	3–12	12
	learning_rate	0.005–0.3	0.256
	min_child_weight	1–10	5
	subsample	0.5–1.0	0.922
	colsample_bytree	0.5–1.0	0.599

abrupt spatial changes in the weights, the local weights were further propagated to neighboring grid cells through Gaussian kernel smoothing and were gradually shrunk toward the global prior weights as observational support decreased.

We define the global prior weight  $\omega_i$  of model  $i$  from its MAE  $\varepsilon_i$  in temporal cross-validation (Sect. 3.1) as

$$\omega_i = \frac{\exp(-\beta\varepsilon_i)}{\sum_{j=1}^M \exp(-\beta\varepsilon_j)} \quad (4)$$

where  $M = 6$  is the number of base models and  $\beta$  is the prior-weight sensitivity parameter. A smaller  $\varepsilon_i$  gives a larger  $\omega_i$ , so models with better overall performance receive higher prior weights. Here,  $\beta$  controls how strongly the prior weights respond to differences in model MAE. We set  $\beta = 1$  to preserve the relative performance differences among models while avoiding excessively concentrated prior weights.

At grid cells with valid observations, we first define the local score of model  $i$  as

$$s_i(x) = \exp(-\alpha|p_i(x) - O(x)|) \quad (5)$$

where  $p_i(x)$  is the prediction of model  $i$  at grid cell  $x$ ,  $O(x)$  is the observed value. Here,  $\alpha$  controls the sensitivity of local weighting to model error. We set  $\alpha = 1$  to preserve the influence of local model-observation mismatch while avoiding excessively sensitive weight adjustments. These local scores are then normalized across all models to obtain the effective local weight at observation-supported grid cells:

$$I_i^{\text{obs}}(x) = \frac{s_i(x)}{\sum_{j=1}^M s_j(x)} \quad (6)$$

To extend the observational constraint smoothly to neighboring locations, we applied Gaussian kernel smoothing to the effective local weights. The kernel is defined as

$$K_h(x, x_n) = \exp\left(-\frac{d_{xy}(x, x_n)^2}{2\sigma_{xy}^2} - \frac{d_z(x, x_n)^2}{2\sigma_z^2}\right) \quad (7)$$

where  $x_n$  denotes a neighboring grid cell,  $d_{xy}(x, x_n)$  is the horizontal distance between  $x$  and  $x_n$ ,  $d_z(x, x_n)$  is the vertical distance, and  $\sigma_{xy}$  and  $\sigma_z$  control the smoothing scales in the horizontal and vertical directions, respectively. The smoothed local weight of model  $i$  is then written as

$$\tilde{l}_i(x) = \frac{\sum_{x_n \in N(x)} K_h(x, x_n) I_i^{\text{obs}}(x_n)}{\sum_{x_n \in N(x)} K_h(x, x_n)} \quad (8)$$

where  $N(x)$  is the set of neighboring grid cells with valid effective local weights.

To quantify the degree of local observational support around each grid cell, we define

$$S(x) = \sum_{x_n \in N(x)} K_h(x, x_n) \quad (9)$$

and then construct an observation-support factor as

$$\rho(x) = \frac{S(x)}{S(x) + c} \quad (10)$$

where  $c$  is a shrinkage parameter. When observational support is strong,  $\rho(x)$  approaches 1 and the final weight is mainly controlled by the smoothed local weight. When observational support is weak,  $\rho(x)$  decreases and the final weight gradually returns toward the global prior weight.

Accordingly, the final weight of model  $i$  at grid cell  $x$  is defined as

$$w_i(x) = \rho(x)\tilde{l}_i(x) + [1 - \rho(x)]\omega_i \quad (11)$$

The final ensemble reconstruction is then calculated as

$$\hat{O}(x) = \sum_{i=1}^M w_i(x)p_i(x) \quad (12)$$

### 2.2.5 Data reconstruction

We produced a global, monthly DO dataset on a regular  $1^\circ \times 1^\circ$  grid and 75 depth levels (0–5, 902 m) spanning from 1960 to 2023. First, we gathered all the predictor fields described in Table 1. Each field was remapped to the target grid and monthly time step consistent with ORAS5. Next, we applied the six optimized machine-learning models (Sect. 2.2.2) at every valid grid cell and time step. Each model ingested the full vector of predictors and returned a DO estimate only where all predictors were available. This yielded six parallel prediction arrays with dimensions  $360$  (longitude)  $\times$   $180$  (latitude)  $\times$   $75$  (depth)  $\times$   $12$  (months)  $\times$   $64$  (years from 1960 to 2023). We then merged these arrays using our spatially coherent dynamic weighting scheme (Sect. 2.2.4). Global prior weights reflected each model's cross-validation skill, whereas locally varying weights were derived from model agreement with available in situ observations. These local weights were then propagated to neighboring grid cells through Gaussian kernel smoothing and gradually shrunk toward the prior weights as observational support decreased. The weighted combination produces a single ensemble DO field for each grid cell and month. We packaged the ensemble field into a NetCDF file with coordinate variables, depth layers, time axes, and global attributes documenting the dataset and methods.

### 2.2.6 Argo oxygen data bias correction

Even after delayed-mode processing and standard quality control, Argo DO profiles are known to be systematically low relative to high-quality ship-based observations. To quantify the influence of a systematic offset in delayed-mode Argo, we produced two global reconstructions using the same machine-learning framework and predictors. The first was a standard reconstruction using CTD, OSD, and delayed-mode Argo profiles. The second was the bias-corrected reconstruction, which was otherwise identical but utilized the CTD, OSD, and delayed-mode Argo values adjusted by adding  $1.69 \mu\text{mol kg}^{-1}$  to every delayed-mode Argo measurement, following Wang et al. (2025). A comparison of the two reconstructions is shown in Sect. 5.5. All the other main results of the paper are based on the bias-corrected reconstruction.

## 3 Model performance

### 3.1 Model temporal cross-validation

We conducted 8-fold temporal cross-validation on each of the six models. In each fold  $f$ , data from eight test years  $\{1960 + f + 8k\}_{k=0}^7$  formed the test set, with the remaining years for training. We trained each model using its optimized hyperparameters (Sect. 2.2.3) on the training set, predicted the DO values for the test years, and computed the mean bias ( $\Delta\text{DO}$ ), mean absolute error (MAE), root-mean-square error

(RMSE), and coefficient of determination ( $R^2$ ) on the held-out data. These metrics collectively provide a comprehensive understanding of the model's predictive accuracy and bias. The results are presented in Tables S3–S6.

$$\text{RMSE} = \sqrt{\frac{1}{n} \sum_{i=1}^n (y_i - \hat{y}_i)^2} \quad (13)$$

$$\text{MAE} = \frac{1}{n} \sum_{i=1}^n |y_i - \hat{y}_i| \quad (14)$$

$$R^2 = 1 - \frac{\sum_{i=1}^n (y_i - \hat{y}_i)^2}{\sum_{i=1}^n (y_i - \bar{y})^2} \quad (15)$$

$$\Delta\text{DO} = \frac{1}{n} \sum_{i=1}^n (y_i - \hat{y}_i) \quad (16)$$

All six learners exhibited consistent skill across the eight temporal folds, with only minor spread in error metrics (Tables S3–S6). LightGBM displayed high stability, with MAEs varying by less than  $1 \mu\text{mol kg}^{-1}$  (10.11–11.04) and RMSEs under  $1.3 \mu\text{mol kg}^{-1}$  (16.38–17.59), yielding an  $R^2$  range of 0.957–0.961. RF delivered the lowest RMSE (15.97–17.27) and highest  $R^2$  (0.958–0.963). In contrast, CatBoost and Hist\_GBT had slightly higher mean errors (MAEs of up to 11.04 and 11.42 and RMSEs of up to 17.57 and 17.99, respectively) and slightly greater inter-fold variability, indicating higher sensitivity to the specific training/test split (Tables S3–S6). Crucially, no model exhibited outlier folds with degraded performance, as all the models maintained MAEs  $< 12 \mu\text{mol kg}^{-1}$  and  $R^2 > 0.95$ . This uniformity across folds confirms strong temporal generalization and validates our choice of an ensemble approach (Bergmeir and Benítez, 2012; Roberts et al., 2017).

### 3.2 Evaluation against independent observations

We evaluated both the ensemble and each individual model against an independent filtered GLODAPv2 dataset. Filtered GLODAPv2 profiles were averaged into the same  $1^\circ \times 1^\circ$  grid and monthly time step as the reconstructions.

Table 3 demonstrates the clear advantage of the BLENDR framework. A stricter sensitivity test using a wider spatiotemporal exclusion criterion yielded very similar validation metrics (Table S7), suggesting that the main evaluation results are not sensitive to the original filtering choice. While the equal-weight ensemble outperformed most individual models, its MAE was still slightly higher than that of RF. This shows that simple averaging does not always outperform the best individual model, because weaker learners can still introduce additional errors. This improved performance is likely related to two reasons. BLENDR used each model's cross-validation skill and further optimized the

weights through the spatially coherent dynamic weighting scheme. Among the individual algorithms, the RF and LightGBM performed best, whereas XGBoost and Hist\_GBT performed at the lower end. All models had absolute biases below  $1.2 \mu\text{mol kg}^{-1}$ . No individual method showed unstable or extremely poor performance in this evaluation, underscoring the robustness of our dynamic weighting in combining complementary strengths and minimizing weaknesses.

### 3.3 Uncertainty estimations

We quantified three distinct contributors to uncertainty in the reconstructed DO field, namely, measurement, grid, and algorithm uncertainty. These components were estimated separately and then combined to provide a first-order global uncertainty estimate.

The measurement uncertainty ( $O_{\text{meas}}$ ) represents the random errors of the in situ dissolved oxygen observations. We adjusted the delayed-mode Argo DO values by adding a constant  $+1.69 \mu\text{mol kg}^{-1}$  (Sect. 2.1.1), following the global bias assessment of Wang et al. (2025). After this bias correction, we treated Argo and CTD/OSD as unbiased on average, and  $O_{\text{meas}}$  represents only the residual random measurement error. We assumed constant uncertainties of  $1 \mu\text{mol kg}^{-1}$  for OSD and CTD and  $3 \mu\text{mol kg}^{-1}$  for Argo, following Ito et al. (2024). We then summarized a representative value across all observations using the root-mean-square of these assigned uncertainties.

The grid uncertainty ( $O_{\text{grid}}$ ) quantifies the error associated with assigning a single value to a  $1^\circ \times 1^\circ$  grid cell. We estimated  $O_{\text{grid}}$  from the dispersion of collocated observations within each grid cell. For each grid cell with at least 10 collocated observations, we computed the within-cell standard deviation as follows:

$$\Delta O_{\text{grid}} = \sigma = \sqrt{\frac{1}{n-1} \sum_{i=1}^n (O_i - \bar{O})^2} \quad (17)$$

where  $O_i$  is the  $i$ th observation in the cell and  $\bar{O}$  is the mean value of the observations. We then averaged  $\sigma$  over all qualifying cells to obtain a single global estimate of  $O_{\text{grid}}$ .

The algorithm uncertainty ( $O_{\text{alg}}$ ) reflects the error introduced by the machine learning reconstruction process. We trained six models (RF, XGBoost, LightGBM, CatBoost, ERT, and Hist\_GBT) using DO observations and environmental factors. Each model was optimized via Bayesian hyperparameter tuning and validated using an 8-fold cross-validation procedure, yielding an MAE for each model, denoted by error1 through error6. We then computed the prior weight for the  $i$ th model using an exponential decay function:

$$\omega_i = \frac{\exp(-\text{error}_i)}{\sum_{j=1}^6 \exp(-\text{error}_j)} \quad (18)$$

and estimated the algorithm uncertainty as the weighted average of the MAE:

$$\Delta O_{\text{alg}} = \sum_{i=1}^6 \omega_i \text{error}_i \quad (19)$$

Finally, the total uncertainty ( $O_{\text{total}}$ ) in the reconstructed dissolved oxygen field is expressed as follows:

$$\Delta O_{\text{total}} = \sqrt{\Delta O_{\text{meas}}^2 + \Delta O_{\text{grid}}^2 + \Delta O_{\text{alg}}^2} \quad (20)$$

Using this framework, the estimated global component uncertainties were  $O_{\text{meas}} = 1.60$ ,  $O_{\text{grid}} = 4.56$ , and  $O_{\text{alg}} = 10.29 \mu\text{mol kg}^{-1}$ , resulting in a combined global uncertainty of  $O_{\text{total}} = 11.37 \mu\text{mol kg}^{-1}$ .

## 4 Intercomparison with existing oxygen products

### 4.1 Comparison with filtered GLODAPv2 observations

Compared with GOBAI (Sharp et al., 2023) and ITO (Ito et al., 2024), BLENDR showed the best overall agreement with the filtered GLODAPv2 reference dataset (Table 4). The comparison was conducted both over the full filtered GLODAPv2 dataset and within the coverage domains of GOBAI and ITO (Table 4). BLENDR achieved the lowest MAE and RMSE and the highest  $R^2$  among the three products, with values of 10.204, 18.139  $\mu\text{mol kg}^{-1}$ , and 0.968, respectively. Within the GOBAI coverage, BLENDR had a lower RMSE and a higher  $R^2$  than GOBAI, although its MAE was slightly higher. Its mean bias was also closer to zero. Within the ITO coverage, BLENDR again showed lower MAE and RMSE and a higher  $R^2$  than ITO, although its mean bias was farther from zero. Overall, these comparisons show that BLENDR compares favorably with existing products both over the full filtered GLODAPv2 comparison set and within their respective coverage domains.

### 4.2 Comparison of mean vertical profile

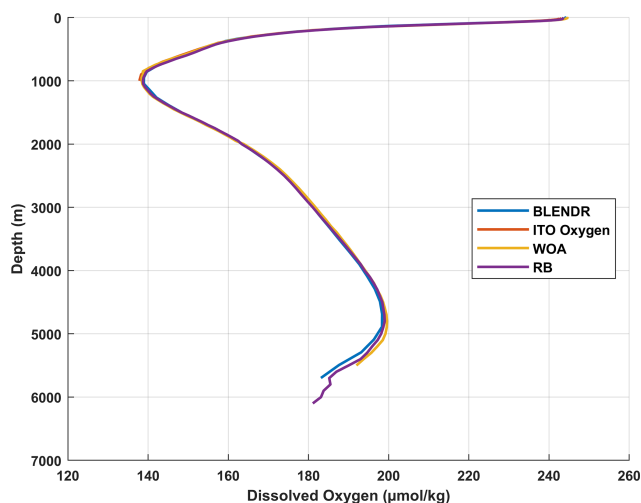
The global mean vertical profile of BLENDR is broadly consistent with those of ITO Oxygen, WOA23, and the DIVA-based product of Roach and Bindoff (RB) over most of the water column (Fig. 2). The four profiles are very close near the surface. In the upper 0–1000 m, BLENDR, ITO, WOA23, and RB remain highly consistent. From about 1000 to 3500 m, the profiles of BLENDR, WOA23, and RB are nearly indistinguishable, indicating that BLENDR reproduces the large-scale deep-ocean oxygen structure well in this depth range. Below 3500 m, the profile of RB remains slightly closer to WOA23, but the differences among the products are still small. Overall, the mean-profile comparison shows that BLENDR remains close to the other products over most of the water column and reproduces the large-scale vertical structure consistently.

**Table 3.** Comparison of ensemble and individual models on the filtered GLODAPv2 dataset. Bold values indicate the best performance for each metric.

Model	MAE ( $\mu\text{mol kg}^{-1}$ )	RMSE ( $\mu\text{mol kg}^{-1}$ )	$R^2$	$\Delta\text{DO}$ ( $\mu\text{mol kg}^{-1}$ )
BLENDR	<b>10.204</b>	<b>18.139</b>	<b>0.968</b>	-0.334
Equal-weight ensemble	10.434	18.302	0.967	-0.214
RF	10.266	18.394	0.966	-0.531
XGBoost	12.136	19.502	0.962	0.270
ERT	11.402	19.620	0.962	-1.167
LightGBM	11.314	18.968	0.964	0.167
Hist_GBT	11.942	19.739	0.962	<b>-0.099</b>
CatBoost	11.549	19.275	0.963	0.431

**Table 4.** Performance comparison of BLENDR, GOBAI, and ITO against filtered GLODAPv2. Bold values indicate the best performance within each paired comparison domain. The GOBAI comparison is evaluated between “GOBAI on filtered GLODAPv2” and “BLENDR in GOBAI coverage”, while the ITO comparison is evaluated between “ITO on filtered GLODAPv2” and “BLENDR in ITO coverage”.

Product	MAE ( $\mu\text{mol kg}^{-1}$ )	RMSE ( $\mu\text{mol kg}^{-1}$ )	$R^2$	$\Delta\text{DO}$ ( $\mu\text{mol kg}^{-1}$ )
BLENDR	10.204	18.139	0.968	-0.334
GOBAI on filtered GLODAPv2	<b>11.101</b>	19.875	0.956	-0.971
BLENDR in GOBAI coverage	11.115	<b>19.658</b>	<b>0.963</b>	<b>-0.470</b>
ITO on filtered GLODAPv2	13.415	22.958	0.951	<b>-0.123</b>
BLENDR in ITO coverage	<b>11.824</b>	<b>19.966</b>	<b>0.964</b>	-0.544

**Figure 2.** Global mean vertical profiles of different dissolved oxygen products (1965–2022). Solid lines show BLENDR (blue), Roach & Bindoff’s reconstruction (purple), ITO Oxygen (orange) and WOA23 climatology (yellow), plotted from the surface down to 6000 m.

#### 4.3 Spatial difference from climatological distribution

Relative to WOA23, BLENDR shows smaller large-scale departures than ITO in the upper layer and broadly comparable differences to RB in the deep layer (Figs. 3 and 4).

Compared with ITO (Fig. 3), BLENDR is closer to WOA23, particularly in the surface layer, and shows smaller differences in many low- and mid-latitude regions. At around 10 m depth, BLENDR shows small differences, generally within  $\pm 2 \mu\text{mol kg}^{-1}$ , except in some high-latitude regions. In comparison, ITO exhibits broader regions where it is lower than WOA23 in the subtropical gyres and more pronounced regions where it is higher than WOA23 under the Antarctic Circumpolar Current. At around 30 m, the differences in BLENDR remain small in most mid-latitude regions, with larger variability near boundary currents. In contrast, ITO again shows larger departures in the subtropics and southern high latitudes. These results indicate that BLENDR is generally closer to WOA23 in the surface ocean. At around 200 m, both BLENDR and ITO Oxygen show larger departures from WOA23, reaching about  $\pm 10 \mu\text{mol kg}^{-1}$  in the tropical and subtropical regions. At around 700 m, BLENDR and WOA23 remain within about  $\pm 8 \mu\text{mol kg}^{-1}$  over large parts of the Atlantic and Pacific basins.

In the comparison with RB, BLENDR shows a similar reduction in differences from WOA23 with increasing depth (Fig. 4). At around 10 m, BLENDR is generally closer to WOA23 than RB, with smaller spatial differences over much of the open ocean. At around 700 m, both BLENDR and RB show relatively large differences from WOA23. At around 1500 m, the differences decrease in both products, and at around 4000 m they decrease further, with both

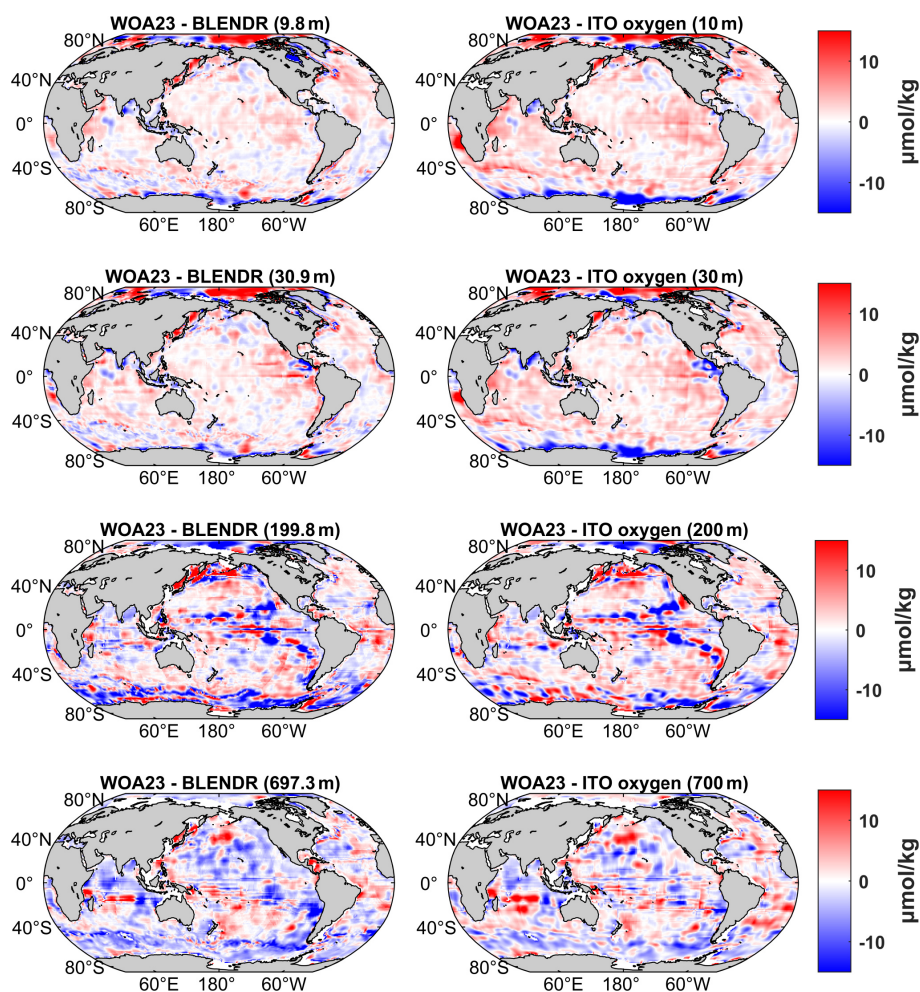


**Figure 3.** Spatial differences from WOA23 at four representative depths for BLENDR and ITO Oxygen. Left panels show WOA23 minus BLENDR at 9.8, 30.9, 199.8, and 697.3 m. Right panels show WOA23 minus ITO Oxygen at 10, 30, 200, and 700 m. Units are  $\mu\text{mol kg}^{-1}$ .

products showing generally smaller differences relative to WOA23. This comparison indicates that BLENDR agrees more closely with WOA23 in the surface layer, while in the deep ocean both BLENDR and RB show reduced differences below about 1500 m.

#### 4.4 Comparison of oxygen content anomaly

BLENDR and ITO Oxygen show a similar multidecadal evolution of upper-ocean oxygen content anomaly during 1965–2020 (Fig. 5), with positive anomalies before the early 1990s, a rapid decline during the 1990s, and persistent negative anomalies after 2000. ITO Oxygen exhibits slightly larger anomaly amplitudes than BLENDR in the earlier part of the record, but the long-term downward trend and the timing of the transition from positive to negative anomalies are similar in both products. This result indicates that BLENDR is consistent with ITO Oxygen in capturing the large-scale decline of upper-ocean oxygen content.

## 5 Global ocean DO distribution and trends

### 5.1 Spatial distributions along the vertical direction

Our reconstruction shows the full vertical extent of historical deoxygenation from the surface ocean to the abyss, providing continuous monthly fields down to 5902 m (Fig. 6a). The surface layer (0.5 m) is generally characterized by high DO concentrations, reflecting air–sea exchange and photosynthetic production (Ryther, 1956; Kolber et al., 2000). The especially high values at high latitudes ( $> 300 \mu\text{mol kg}^{-1}$ ) are consistent with enhanced oxygen solubility in colder waters. At approximately 200 m, strong horizontal contrasts emerge, with broad low-oxygen regions in the eastern tropical Pacific and northern Indian Ocean ( $< 160 \mu\text{mol kg}^{-1}$ ), while subtropical regions remain relatively oxygenated ( $> 200 \mu\text{mol kg}^{-1}$ ). This rapid decrease reflects diminished gas exchange and ongoing microbial respiration (Keeling et al., 2010; Schmidtke et al., 2017). At approximately 850 m, the lowest DO concentrations are most evident, with the concentrations

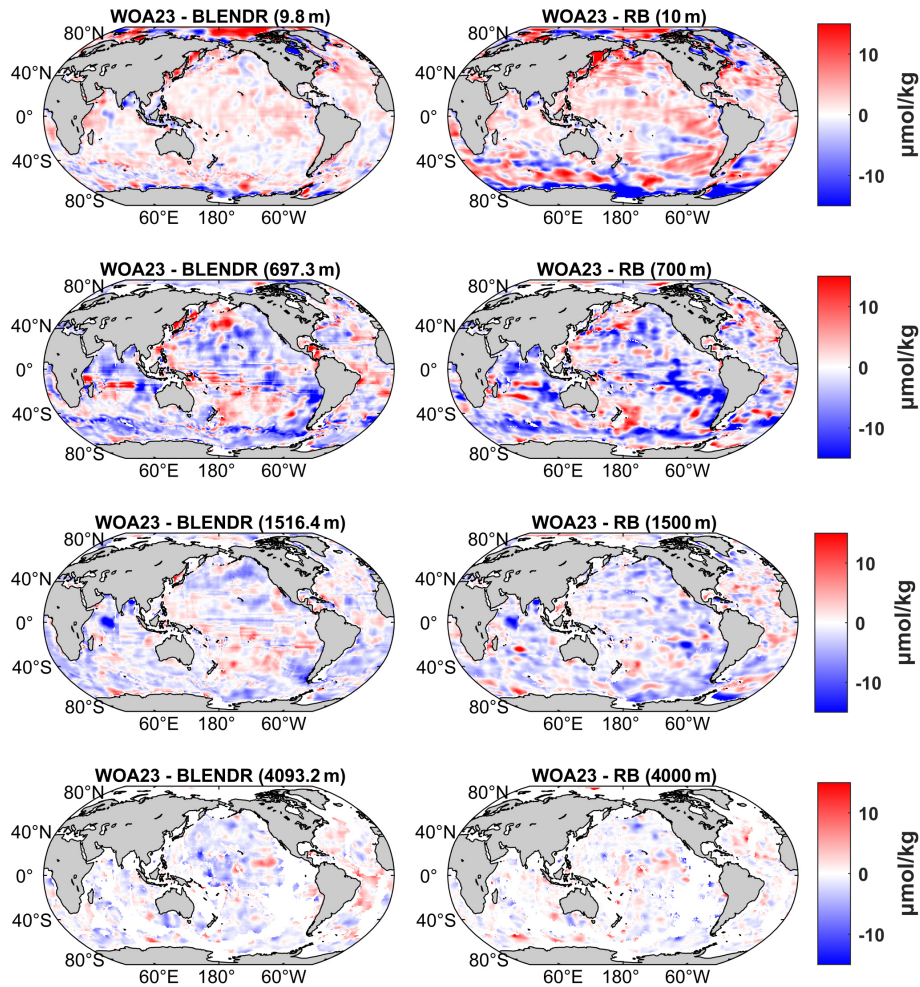


**Figure 4.** Spatial differences from WOA23 at four representative depths for BLENDR and the Roach and Bindoff (RB) product. Left panels show WOA23 minus BLENDR at 9.8, 697.3, 1516.4, and 4093.2 m. Right panels show WOA23 minus RB at 10, 700, 1500, and 4000 m. Units are  $\mu\text{mol kg}^{-1}$ .

in the eastern Pacific and northern Indian Ocean decreasing below  $150 \mu\text{mol kg}^{-1}$ , whereas the North Atlantic (NA) mid-depth ocean maintains higher concentrations ( $180\text{--}200 \mu\text{mol kg}^{-1}$ ). In the bathypelagic zone ( $\sim 4000$  m), DO becomes spatially uniform ( $180\text{--}200 \mu\text{mol kg}^{-1}$ ) across basins, which is consistent with the large-scale deep-water mass structure (Talley, 2013). Overall, along the water column, the DO concentration peaks at the surface and reaches a local minimum of approximately  $139 \mu\text{mol kg}^{-1}$  near the classical OMZ at approximately 1000 m but then slowly increases toward  $200 \mu\text{mol kg}^{-1}$  at approximately 4500 m (Fig. 6b).

The global mean DO trend from 1960 to 2023 was negative at nearly all depths, with the strongest deoxygenation in the subsurface ocean and weaker trends in the surface and deep ocean (Fig. 6b). While the deoxygenation rate was low ( $-0.04 \mu\text{mol kg}^{-1} \text{yr}^{-1}$ ) at the surface, the decline accelerated greatly below 60 m, reaching its most negative values

between 150 and 200 m ( $-0.12 \mu\text{mol kg}^{-1} \text{yr}^{-1}$ ). This pattern reflects an amplification of shallow subsurface oxygen loss, most likely driven by stronger stratification that inhibits ventilation exchange and by increased microbial respiration (Keeling et al., 2010; Schmidtko et al., 2017).

## 5.2 Depth-basin patterns in the OMZ area

Over the past six decades, the OMZ ( $\text{DO} < 60 \mu\text{mol kg}^{-1}$ ) has existed primarily at depths between 100 and 2000 m, but its vertical structure and magnitude vary strongly between basins (Fig. 7). In the global mean profile, the total OMZ area increases from the surface to a broad maximum near 800 m and then decreases toward deeper waters. In the North Pacific (NP), the OMZ is thickest, with a wide band of large area between approximately 800 and 1200 m, which is consistent with slow intermediate-water ventilation and long residence times that allow for respiration to consume oxygen (Karstensen et al., 2008; Paulmier and Ruiz-Pino, 2009). In

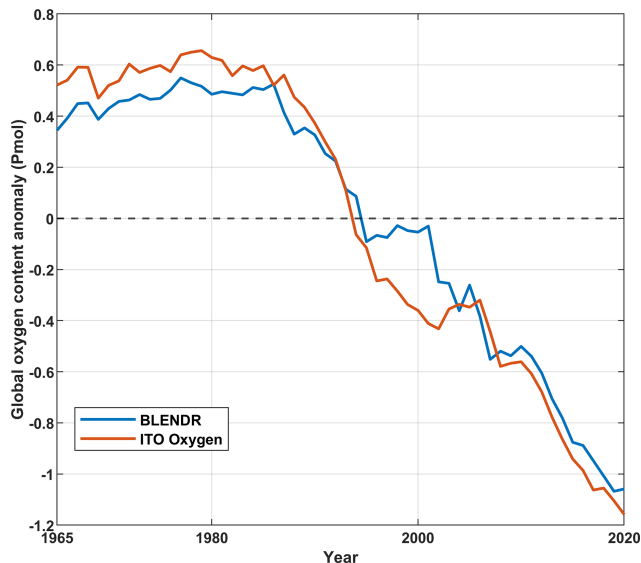


**Figure 5.** Global oxygen content anomaly in the upper 1000 m from BLENDR and ITO Oxygen during 1965–2020. The blue line denotes BLENDR and the orange line denotes ITO Oxygen. Anomalies are expressed in Pmol relative to the mean over the comparison period.

the North Indian (NI), by contrast, the largest OMZ area is much shallower, between approximately 100 and 1000 m, reflecting a combination of weak thermocline ventilation and strong export production in the Arabian Sea and Bay of Bengal that produces very intense hypoxia (Naqvi et al., 2006; Keeling et al., 2010). The Equatorial Pacific (EP) and Equatorial Atlantic (EA) have thinner OMZ layers centered at approximately 300–600 m. The OMZ in the EP is located primarily in the eastern ocean because of relatively stagnant cyclonic gyres north and south of the equator in the east subsurface layers, which are poorly ventilated (Keeling et al., 2010). In the Atlantic, the OMZ area is much smaller than that in the Pacific, which is consistent with stronger ventilation of the Atlantic thermocline and intermediate waters (Stramma et al., 2008; Talley, 2013).

These basin differences are also reflected in the vertical profiles of the OMZ extent. OMZ extents have distinct depth profiles across the regions: the NP, EP, and EA are characterized by a single local maximum, whereas the North Indian Ocean (including the Arabian Sea and Bay of Bengal) exhibits two local maxima, suggesting periodic intrusions of oxygen-rich water (Jain et al., 2017; Sarma and Udaya Bhaskar, 2018). The high productivity in the western Arabian Sea region leads to increased oxygen consumption (Acharya and Panigrahi, 2016), whereas the oxygen-rich Somali Current, approximately 500 m deep, introduces oxygen, particularly during summer (Zhang et al., 2022), resulting in weaker OMZs at this depth. Persian Gulf Water (PGW) in the Bay of Bengal contributes to a modest increase in oxygen at 350–450 m (Jain et al., 2017), resulting in a reduced OMZ.

These intrusions disrupt the continuity of OMZs, leading to the dual-minima pattern observed in these regions. This phenomenon highlights the complex and dynamic nature of OMZ distribution and its susceptibility to various oceanographic processes.

Over the 1960–2023 period, the OMZ area profile gradually expanded across nearly all depths in terms of the global mean and most basins (Fig. 7). These changes indicate a significant shift in the vertical distribution and extent of low-oxygen seawater globally over the past six decades. Specifically, the global OMZ extent growth rate was highest at 400–1000 m because of expansion across all regions, with its peak at 600–700 m due to expansion in the EP and NP. Therefore, while the largest OMZ extent was approximately 900 m, shifts to the much shallower 600–700 m layer are likely in the future. After this peak, the horizontal expansion rate of the OMZ decreased, with the lowest rates occurring at 1300–1600 m. However, the expansion rates increased again beyond 1600 m because of growth in the NP.

### 5.3 Basin-scale deoxygenation and spatial trend patterns

Deoxygenation was more negative after 2010 across all major ocean basins, indicating stronger recent oxygen loss over the 1960–2023 record (Fig. 8). During the period from 1960 to 2010, the deoxygenation rates were generally modest. The greatest loss ( $91.4 \pm 17.7$  Tmol per decade) occurred in the NP, followed by the Southern Ocean (SO) ( $86.8 \pm 10.5$  Tmol per decade) and South Atlantic (SA) ( $68.3 \pm 10.4$  Tmol per decade). In the Southern Indian (SI) and South Pacific (SP) basins, the deoxygenation trends from 1960 to 2010 were almost negligible. This likely reflects the much sparser observational coverage in the Southern Hemisphere during the early record than during the Argo era.

In the period after 2010, oxygen loss trends significantly increased across all the basins. The NA loss increased by more than a factor of 16 to  $299.1 \pm 45.8$  Tmol per decade. The SA and NP both exceeded 240 Tmol per decade. The Arctic Ocean (AO) accelerated from near zero to  $78.6 \pm 18.1$  Tmol per decade. This recent acceleration of oxygen loss is attributed to amplified warming of Atlantic inflow from the 2000s to the 2010s, which reduces oxygen solubility and advects low-oxygen waters into the basin (Wu et al., 2025).

The spatial distribution of dissolved oxygen trends during 2011–2023 shows widespread deoxygenation in both the upper layer (0–1516 m) and the deep layer (1516–5902 m), with the upper layer exhibiting stronger magnitudes and greater spatial heterogeneity (Fig. 9). Compared with 1960–2010, the 2011–2023 period exhibits much stronger and more spatially heterogeneous linear trend patterns in both layers, whereas the earlier period is characterized by weaker and more spatially uniform changes.

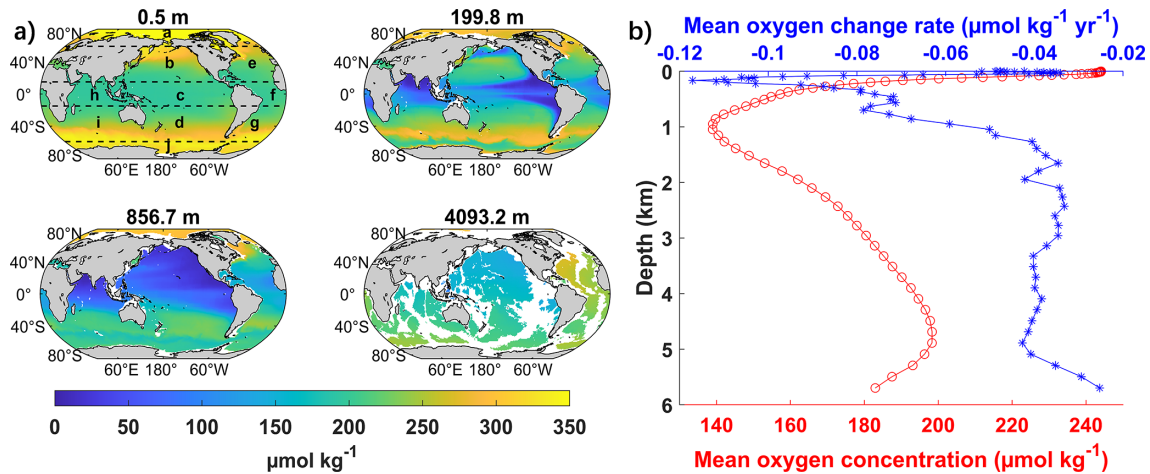


**Figure 6.** Global distribution and vertical structure of dissolved oxygen. **(a)** Climatological mean dissolved oxygen concentration at four representative depths (0.5, 199.8, 856.7, and 4093.2 m) from the reconstructed global product. Letters indicate the ten regions: (a) Arctic Ocean (AO), (b) North Pacific (NP), (c) Equatorial Pacific (EP), (d) South Pacific (SP), (e) North Atlantic (NA), (f) Equatorial Atlantic (EA), (g) South Atlantic (SA), (h) Equatorial Indian (EI), (i) South Indian (SI), and (j) Southern Ocean (SO). This regionalization scheme is adopted from Schmidtko et al. (2017). **(b)** Global mean vertical profiles of the dissolved oxygen concentration (red;  $\mu\text{mol kg}^{-1}$ ) and its long-term linear change rate (blue;  $\mu\text{mol kg}^{-1} \text{yr}^{-1}$ ).

Although negative trends dominate much of the Pacific, Atlantic, and Southern oceans during 2011–2023, several spatially confined regions of positive trends are also evident. These include the eastern equatorial Pacific (Espinoza-Morriberón et al., 2019), the Southern Ocean (Iida et al., 2013; Morrison et al., 2022), and the North Indian Ocean (Narvekar et al., 2025; Nayak et al., 2025). Some of these localized increases may reflect interannual to decadal variability over the short 2011–2023 period rather than persistent long-term change. These spatial patterns are nevertheless broadly consistent with previous regional studies linking oxygen increases to variability in circulation, ventilation, mixing, and oxygen supply (Karstensen et al., 2008; Espinoza-Morriberón et al., 2019; Busecke et al., 2019; Duteil et al., 2021; Morrison et al., 2022; Narvekar et al., 2025; Nayak et al., 2025). Overall, deoxygenation remains the dominant large-scale signal during 2011–2023, while regional oxygen increases are confined to a few dynamically distinct areas.

#### 5.4 Hemispheric seasonal variability in dissolved oxygen

Along the water column, the seasonal amplitude was strongest in the surface layer, which responds rapidly to the seasonal changes in air–sea gas exchange, surface heating and cooling, and biologically driven production and respiration. In contrast, the seasonal cycles in the thermocline and intermediate ocean ( $\sim 100$ – $1500$  m) were substantially weaker, with anomalies typically  $\pm 1 \mu\text{mol kg}^{-1}$ , and those in the deep ocean ( $> 1500$  m) were nearly constant throughout the year, with amplitudes below  $0.1 \mu\text{mol kg}^{-1}$  (Fig. 10).

This rapid vertical decline in seasonality is consistent with the dominant control mechanisms in the ocean interior. Away from the surface, oxygen is mainly controlled by the ventilation of intermediate waters and by the slow remineralization of sinking organic matter. These processes evolve on multiyear to decadal time scales; thus, these water masses respond weakly to the seasonal cycle (Keeling et al., 2010; Talley, 2013). At abyssal depths, water masses are ventilated in high-latitude formation regions and subsequently spread via slow interior circulation; thus, oxygen variability is controlled mainly by large-scale and long-term transport changes (Oschlies et al., 2018).

Comparing 1960–2010 with 2011–2023, the NH surface DO amplitude intensified, whereas the SH weakened. This hemispheric contrast is consistent with the direct dependence of oxygen on temperature and with the positive correlation between changes in the seasonal amplitude of surface DO and SST (Fig. S4). In recent decades, the sea surface temperature (SST) seasonal amplitudes in large parts of the Northern Hemisphere have increased, whereas in the Southern Ocean, the SST seasonal cycle has shown robust weakening since the 1950s (Fig. S5). Upper-ocean temperature seasonal amplitudes generally increased in the AO and other northern basins but weakened in the Southern Ocean. This pattern is consistent with the opposing NH–SH changes in DO seasonality from our reconstruction.

The Northern Hemisphere (NH) displays a larger seasonal amplitude than the Southern Hemisphere (SH), with peak anomalies in the surface and mid-layer ocean approximately 50 % greater. A main contributor is the larger NH seasonal temperature range than the SH, which amplifies the seasonal cycle of oxygen solubility and therefore the sea-

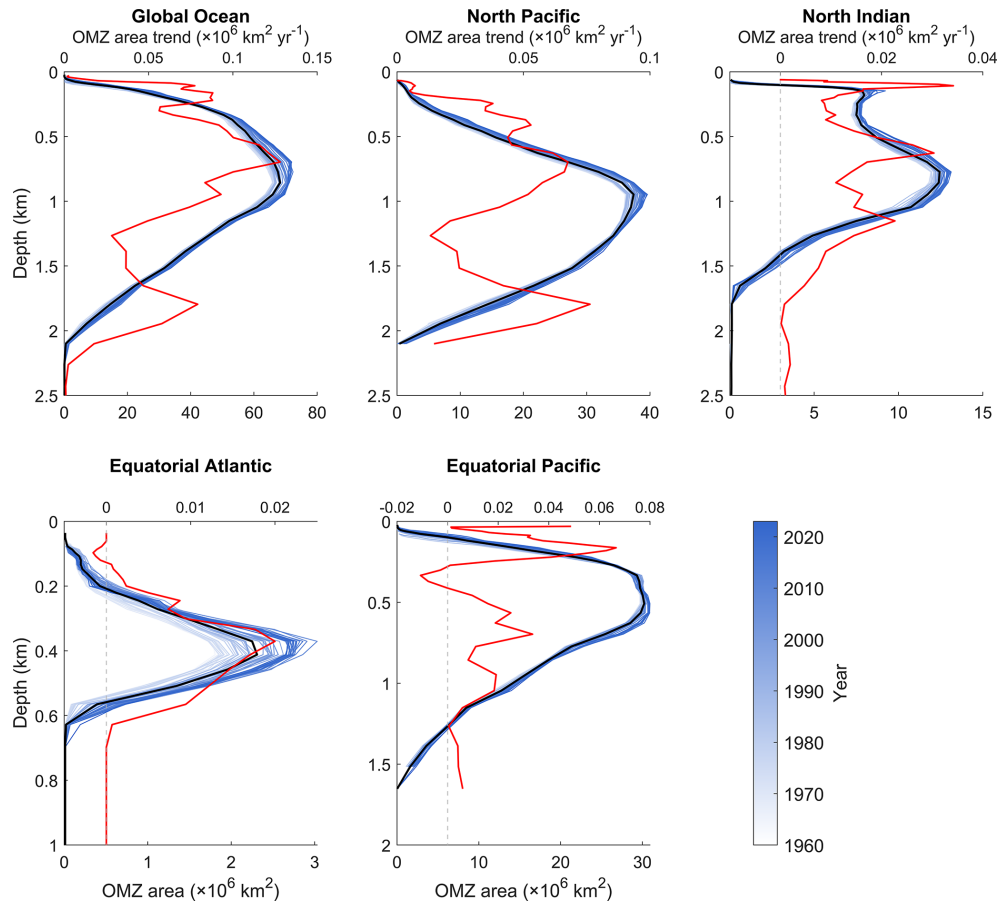


**Figure 7.** Vertical evolution of the OMZ area across major ocean basins during 1960–2023. Vertical profiles of the annual OMZ area (blue lines; threshold =  $60 \mu\text{mol kg}^{-1}$ ) for the global ocean and four major basins: North Pacific, North Indian, Equatorial Atlantic, and Equatorial Pacific. Individual blue curves represent yearly OMZ area profiles, with color shading indicating the year (1960–2023). The black curves show the long-term mean OMZ area at each depth. The red curves denote the linear trend in the OMZ area with depth ( $\times 10^6 \text{ km}^2 \text{ yr}^{-1}$ ), highlighting the depth-dependent expansion or contraction of low-oxygen waters. Here, the North Indian includes the Equatorial Indian labeled h in Fig. 6a, together with the Bay of Bengal and Arabian Sea.

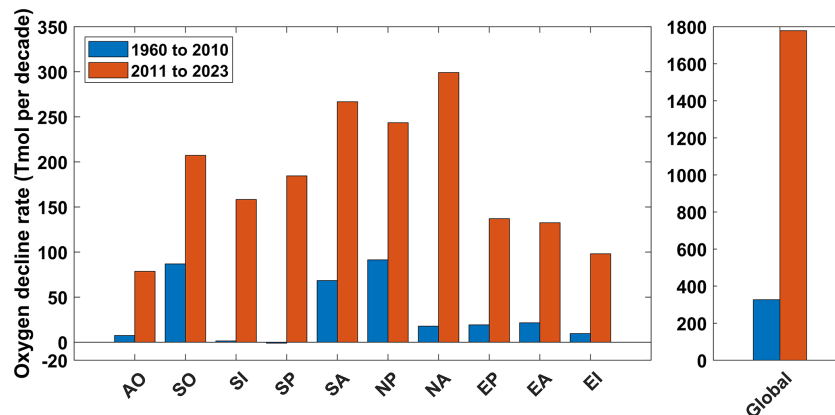


**Figure 8.** Decline in oxygen rates across major ocean basins. Decadal oxygen decline rates are shown for ten individual ocean basins and for the global ocean and were estimated separately for 1960–2010 (blue) and 2011–2023 (orange).

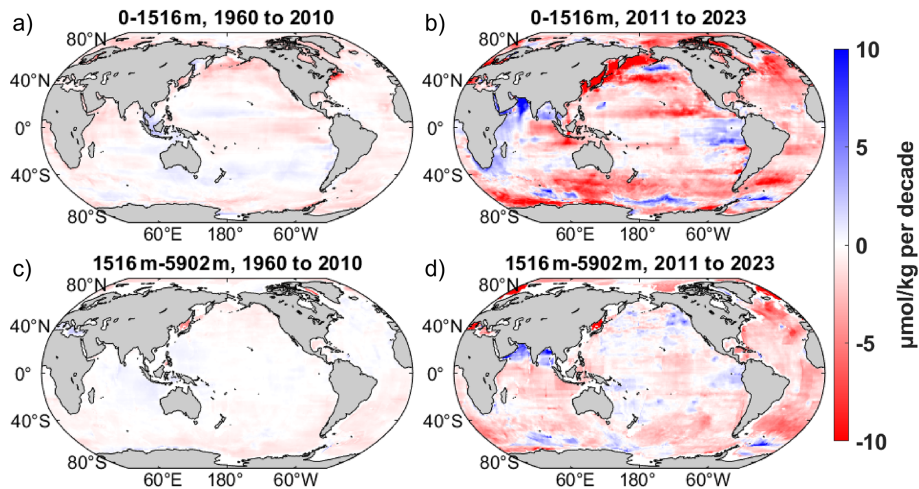


**Figure 9.** Spatial distribution of dissolved oxygen trends for the upper layer (0–1516 m) and deep layer (1516–5902 m) during 1960–2010 and 2011–2023. Panels (a) and (b) show the upper-layer trends for 1960–2010 and 2011–2023, respectively, and panels (c) and (d) show the corresponding deep-layer trends. Trends are expressed in  $\mu\text{mol kg}^{-1}$  per decade. Positive values indicate oxygen increase, and negative values indicate oxygen decrease.

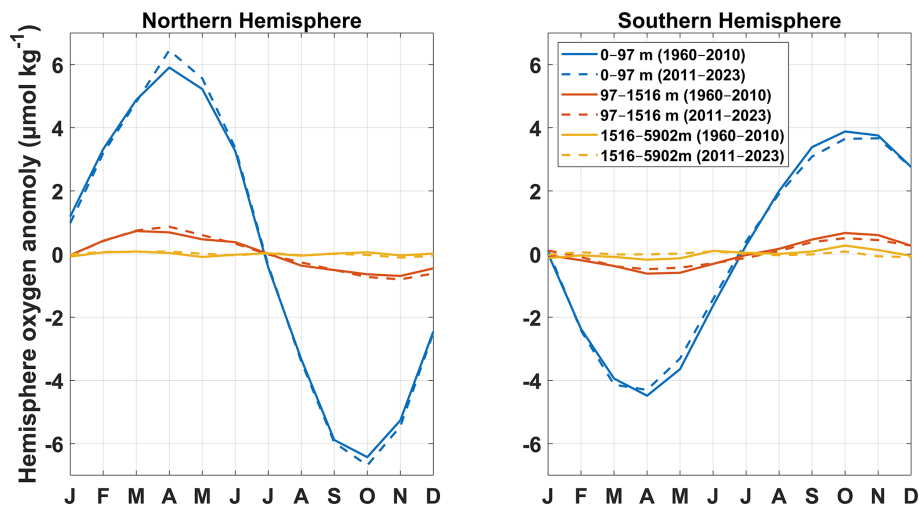


**Figure 10.** Climatological seasonal cycle of hemispheric mean dissolved-oxygen anomalies. The left panel shows the Northern Hemisphere and the right panel shows the Southern Hemisphere. The blue lines denote the surface layer (0–97 m), the red lines denote the thermocline and intermediate layer (97–1516 m), and the yellow lines denote the deep ocean (1516–5902 m). The solid lines represent anomalies from 1960 to 2010, and the dashed lines represent anomalies from 2011 to 2023.

sonal cycle of oxygen saturation capacity (Fig. S5). Biological processes further enhance these differences. Satellite chlorophyll-*a* climatology indicates that the seasonal amplitude of phytoplankton biomass is generally larger at mid- and high northern latitudes than at corresponding southern latitudes (Mao et al., 2020), consistent with a stronger seasonal DO response in the NH. Phytoplankton blooms can drive transient surface DO supersaturation in spring, whereas warmer summer conditions can increase heterotrophic respiration (Frajka-Williams et al., 2009; Carstensen et al., 2014). Argo-based analyses show that, although both hemispheres exhibit enhanced upper-ocean stratification in their respec-

tive summer seasons, the NH typically shows stronger stratification maxima than the SH (Roch et al., 2023), which limits resupply and intensifies late-summer and early-fall DO minimum (Rippeth et al., 2024).

### 5.5 Effect of Argo bias correction on the reconstructed oxygen estimates

The global time series from 1960 to 2023 confirms a long-term and large-scale decline in total dissolved oxygen content (Fig. 11a). Over the full analysis period, both our standard and bias-corrected reconstruction methods indi-

cate a persistent decline, with total losses of  $5.4 \pm 0.5$  and  $4.1 \pm 0.4$  Pmol, respectively. This corresponds to overall decreases of  $2.3 \pm 0.2\%$  and  $1.8 \pm 0.2\%$ , respectively. This magnitude of loss is consistent with prior synthesis estimates of historical deoxygenation, such as approximately  $4.8 \pm 2.1$  Pmol of oxygen loss since 1960 by Schmidtko et al. (2017) and an overall  $\sim 2\%$  decrease in oxygen in the late 20th century by Helm et al. (2011).

The Argo bias correction produces only modest changes in the reconstructed oxygen fields and does not substantially affect the long-term deoxygenation rates (Fig. 11a). Both the standard and the bias-corrected reconstructions strongly agree prior to 2005, when the observations are constrained mainly by ship-based CTD and OSD measurements. After 2005, when the Argo observations became a significant contributor, the reconstruction that incorporates bias-corrected Argo data yielded a slightly higher global mean oxygen content than the uncorrected version did. Consequently, the bias-corrected reconstruction showed a greater global oxygen content in recent years. Vertically, the greatest differences occurred above 2000 m, where the difference mostly ranged from  $-0.4$  to  $-0.6 \mu\text{mol kg}^{-1}$  (Fig. 11b), due to dense Argo float sampling and strong optode biases at this depth. Beyond 2000 m, where sampling mainly comprised sparse ship-based measurements, the difference decreased to  $-0.2 \mu\text{mol kg}^{-1}$ , and below approximately 3500 m, the two reconstructions were almost indistinguishable. In summary, the Argo bias correction improves cross-platform consistency but has only a limited influence on global and basin-scale conclusions drawn from the reconstruction.

## 6 Data availability

The reconstructed global monthly dissolved oxygen dataset produced in this study is publicly available in NetCDF format via Zenodo at <https://doi.org/10.5281/zenodo.19705526> (Han and Zhou, 2026) under a Creative Commons Attribution 4.0 license. Source DO profile observations were obtained from the International Argo Program and the national programs that contribute to Argo (<https://argo.ucsd.edu>, last access: 5 March 2025), the World Ocean Database 2023 (WOD) maintained by the U.S. National Oceanic and Atmospheric Administration (NOAA; <https://www.ncei.noaa.gov/products/world-ocean-database>, last access: 5 March 2025), and the Global Ocean Data Analysis Project v2.2023 (GLODAPv2; [https://www.ncei.noaa.gov/access/ocean-carbon-acidification-data-system/oceans/GLODAPv2\\_2023](https://www.ncei.noaa.gov/access/ocean-carbon-acidification-data-system/oceans/GLODAPv2_2023), last access: 5 March 2025). Environmental predictor fields were drawn from the ORAS5 ocean reanalysis provided by the European Centre for Medium-Range Weather Forecasts (ECMWF; <https://cds.climate.copernicus.eu/datasets/reanalysis-oras5>, last access: 5 March 2025).

## 7 Conclusion and discussion

Our study generated a global  $1^\circ \times 1^\circ$  monthly DO dataset from 1960 to 2023, which extends to 5902 m, achieved through the BLENDR framework. BLENDR integrates six tree-based learners: Random Forest, XGBoost, LightGBM, CatBoost, ERT and Hist\_GBT. These models are optimized using Bayesian optimization and combined via a spatially coherent dynamic weighting scheme. Our ensemble moves well beyond simpler blends and applies a weighting scheme that combines global prior model skill with locally constrained error information, while propagating local weights through Gaussian kernel smoothing and shrinking them toward the prior weights as observational support decreases. As a result, our reconstruction achieved lower MAEs and RMSEs than those of any individual model or equal-weight ensemble on the independent filtered GLODAPv2 dataset and reproduces the large-scale vertical and seasonal structure, including sharp oxycline features and deep ocean signals.

The vertical deoxygenation profile revealed accelerating oxygen loss between 150 and 200 m at rates of approximately  $-0.12 \mu\text{mol kg}^{-1} \text{yr}^{-1}$ , whereas surface decreases remained modest ( $-0.04 \mu\text{mol kg}^{-1} \text{yr}^{-1}$ ). Consistent with this, the OMZ area expanded at nearly all depths, with the strongest growth occurring between approximately 400 and 1000 m and a maximum near 600–700 m, which is driven largely by the Equatorial and North Pacific OMZs, whereas weaker yet still positive trends occurred in the deeper North Pacific below 1600 m. Since 2010, basin-scale trends have accelerated strongly, particularly in the NA and AO, and most other basins have transitioned from weak or negligible trends to substantial oxygen loss, which is consistent with observations of rising temperature, strengthening stratification (Matear and Hirst, 2003; Solomon et al., 2021) and with the deoxygenation of Atlantic inflow feeding the AO (Wu et al., 2025). In the Southern Indian and South Pacific basins, deoxygenation remained weak or even locally positive from 1960 to 2010 (Stramma et al., 2010) but intensified sharply from 2011 to 2023, indicating that these basins shifted from relatively stable oxygen conditions to rapid loss in step with recent upper-ocean warming and circulation changes (Schmidtko et al., 2017; Oschlies et al., 2018).

Our analysis of hemispheric DO seasonality revealed that the Northern Hemisphere exhibits seasonal peak anomalies that are approximately 50 % greater than those in the Southern Hemisphere in both the surface and thermocline layers. This asymmetry arises primarily from the greater seasonal cycle of upper-ocean temperature in the Northern Hemisphere, which amplifies the seasonal cycle of oxygen solubility, while biological and physical processes further sharpen the extremes: spring phytoplankton blooms drive transient surface supersaturation, and warmer, more strongly stratified summer conditions favor heterotrophic respiration and the development of late-summer to early-fall oxygen minima

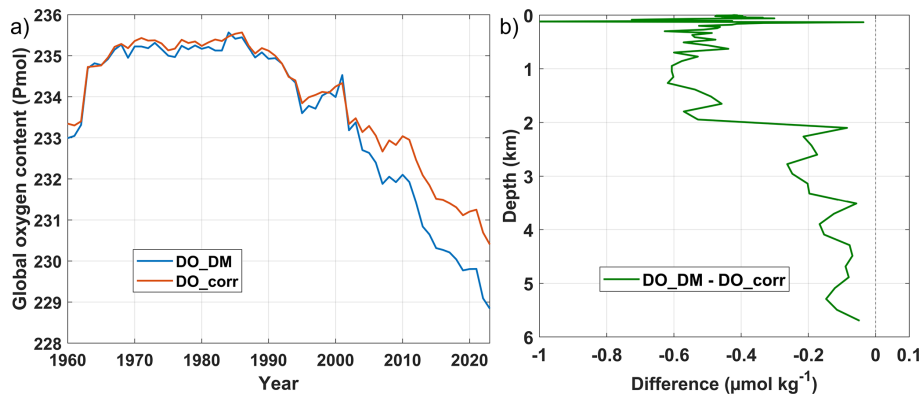


**Figure 11.** Comparison of global ocean oxygen content and annual mean climatology with and without Argo DO bias correction. **(a)** Time series of globally integrated ocean oxygen content from 1960 to 2023 based on two reconstructions that use the same machine-learning framework applied to observational oxygen profiles. The blue curve (DO\_DM) used oxygen measurements from the CTD, OSD, and delayed-mode Argo profiles. The red curve (DO\_corr) used the same inputs but applied a  $+1.69 \mu\text{mol kg}^{-1}$  bias correction to all the Argo DO profiles following Wang et al. (2025). **(b)** Annual mean vertical profile of the difference between the two reconstructions (DO\_DM – DO\_corr).

(Frajka-Williams et al., 2009; Carstensen et al., 2014; Rippeh et al., 2024).

A further contribution of this work is the explicit assessment of how Argo oxygen biases propagate into machine-learning reconstructions. By training two parallel ensembles, one using delayed-mode Argo DO together with CTD/OSD profiles (DO\_DM) and the other applying a uniform  $+1.69 \mu\text{mol kg}^{-1}$  correction to all Argo DO profiles (DO\_corr), we directly quantified the sensitivity of global oxygen inventories and trends to this widely used bias adjustment. This comparison highlights that the recent correction in delayed-mode Argo does not significantly affect the deoxygenation trend in global and regional oceans, which enhances the reliability of long-term, observation-constrained reconstructions.

We note several limitations and avenues for improvement. The  $1^\circ \times 1^\circ$  grid smooths small-scale features such as narrow boundary currents. In addition, although ORAS5 provides dynamically consistent physical predictor fields for the reconstruction, uncertainties in its temperature, salinity, and circulation fields can still propagate into the reconstructed dissolved oxygen through the learned relationships between physical predictors and oxygen. This issue is likely more important in the deep ocean, where direct oxygen observations become much sparser below 2000 m and the reconstruction depends more strongly on the large-scale structure represented by the predictor fields. Because all six models share the same ORAS5 inputs, this source of uncertainty is partly structural and cannot be fully reduced by ensemble weighting. Our current uncertainty estimate does not include predictor uncertainty from ORAS5 and may therefore underestimate total uncertainty in poorly observed deep-ocean regions. Even after a constant bias correction was applied to delayed-mode Argo oxygen, residual sensor biases and calibration uncertainties in biogeochemical Argo (BGC-Argo)

profiles still propagated into our training data, especially around steep oxyclines (Bittig and Körtzinger, 2017; Bittig et al., 2018; Gouretski et al., 2024). Future work should incorporate more precisely calibrated Argo data, finer regional grids, and uncertainty propagation from physical predictor fields.

Overall, our dataset offers a unified, long-term view of ocean deoxygenation from the surface to the abyss and, by extending coverage into the bathypelagic realm, fills a critical observational void that enables studies of deep-ocean oxygen dynamics. Packaging in NetCDF with documented uncertainties provides a benchmark for Earth system models and a foundation for impact studies on marine habitats and biogeochemical cycles and invites the community to explore trends, calibrate models and guide policies on ocean health under climate change.

**Supplement.** The supplement related to this article is available online at <https://doi.org/10.5194/essd-18-3757-2026-supplement>.

**Author contributions.** MH and YZ conceived and designed the study. MH performed the research and wrote the initial draft of this paper. MH, XX, and YZ reviewed and edited the paper.

**Competing interests.** At least one of the (co-)authors is a member of the editorial board of *Earth System Science Data*. The peer-review process was guided by an independent editor, and the authors also have no other competing interests to declare.

**Disclaimer.** Publisher's note: Copernicus Publications remains neutral with regard to jurisdictional claims made in the text, published maps, institutional affiliations, or any other geographical rep-

resentation in this paper. The authors bear the ultimate responsibility for providing appropriate place names. Views expressed in the text are those of the authors and do not necessarily reflect the views of the publisher.

**Acknowledgements.** This research was supported by the National Natural Science Foundation of China (grant no. 42276201), and the National Key Research and Development Program of China (grant no. 2023YFF0805004). The authors also thank the International Argo Program and the national programs for providing Argo data (<https://argo.ucsd.edu>, last access: 5 March 2025), the National Oceanic and Atmospheric Administration (NOAA) for providing WOD data (<https://www.ncei.noaa.gov/products/world-ocean-database>, last access: 5 March 2025), and the European Centre for Medium-Range Weather Forecasts (ECMWF) for providing the ORAS5 data (<https://cds.climate.copernicus.eu/datasets/reanalysis-oras5>, last access: 5 March 2025).

**Financial support.** This research has been supported by the National Natural Science Foundation of China (grant no. 42276201) and the National Key Research and Development Program of China (grant no. 2023YFF0805004).

**Review statement.** This paper was edited by Sabine Schmidt and reviewed by two anonymous referees.

## References

- Acharya, S. S. and Panigrahi, M. K.: Eastward shift and maintenance of Arabian Sea oxygen minimum zone: Understanding the paradox, *Deep-Sea Res. Pt. I*, 115, 240–252, <https://doi.org/10.1016/j.dsr.2016.07.004>, 2016.
- Akiba, T., Sano, S., Yanase, T., Ohta, T., and Koyama, M.: Optuna: A Next-generation Hyperparameter Optimization Framework, in: Proceedings of the 25th ACM SIGKDD International Conference on Knowledge Discovery & Data Mining, 2623–2631, <https://doi.org/10.1145/3292500.3330701>, 2019.
- Bergmeir, C. and Benítez, J. M.: On the use of cross-validation for time series predictor evaluation, *Inform. Sciences*, 191, 192–213, <https://doi.org/10.1016/j.ins.2011.12.028>, 2012.
- Berman-Frank, I., Chen, Y.-B., Gao, Y., Fennel, K., Follows, M. J., Milligan, A. J., and Falkowski, P. G.: Feedbacks Between the Nitrogen, Carbon and Oxygen Cycles, in: *Nitrogen in the Marine Environment*, Elsevier, 1537–1563, <https://doi.org/10.1016/B978-0-12-372522-6.00035-9>, 2008.
- Bittig, H. C. and Körtzinger, A.: Technical note: Update on response times, in-air measurements, and in situ drift for oxygen optodes on profiling platforms, *Ocean Sci.*, 13, 1–11, <https://doi.org/10.5194/os-13-1-2017>, 2017.
- Bittig, H. C., Körtzinger, A., Neill, C., Van Ooijen, E., Plant, J. N., Hahn, J., Johnson, K. S., Yang, B., and Emerson, S. R.: Oxygen Optode Sensors: Principle, Characterization, Calibration, and Application in the Ocean, *Front. Mar. Sci.*, 4, 429, <https://doi.org/10.3389/fmars.2017.00429>, 2018.
- Bopp, L., Resplandy, L., Orr, J. C., Doney, S. C., Dunne, J. P., Gehlen, M., Halloran, P., Heinze, C., Ilyina, T., Séférian, R., Tjiputra, J., and Vichi, M.: Multiple stressors of ocean ecosystems in the 21st century: projections with CMIP5 models, *Biogeosciences*, 10, 6225–6245, <https://doi.org/10.5194/bg-10-6225-2013>, 2013.
- Breiman, L.: Random Forests, *Mach. Learn.*, 45, 5–32, <https://doi.org/10.1023/A:1010933404324>, 2001.
- Breitbart, D., Levin, L. A., Oschlies, A., Grégoire, M., Chavez, F. P., Conley, D. J., Garçon, V., Gilbert, D., Gutiérrez, D., Isensee, K., Jacinto, G. S., Limburg, K. E., Montes, I., Naqvi, S. W. A., Pitcher, G. C., Rabalais, N. N., Roman, M. R., Rose, K. A., Seibel, B. A., Telszewski, M., Yasuhara, M., and Zhang, J.: Declining oxygen in the global ocean and coastal waters, *Science*, 359, eaam7240, <https://doi.org/10.1126/science.aam7240>, 2018.
- Brunsdon, C., Fotheringham, A. S., and Charlton, M. E.: Geographically Weighted Regression: A Method for Exploring Spatial Nonstationarity, *Geogr. Anal.*, 28, 281–298, <https://doi.org/10.1111/j.1538-4632.1996.tb00936.x>, 1996.
- Busecke, J. J. M., Resplandy, L., and Dunne, J. P.: The Equatorial Undercurrent and the Oxygen Minimum Zone in the Pacific, *Geophys. Res. Lett.*, 46, 6716–6725, <https://doi.org/10.1029/2019GL082692>, 2019.
- Carstensen, J., Andersen, J. H., Gustafsson, B. G., and Conley, D. J.: Deoxygenation of the Baltic Sea during the last century, *P. Natl. Acad. Sci. USA*, 111, 5628–5633, <https://doi.org/10.1073/pnas.1323156111>, 2014.
- Chen, T. and Guestrin, C.: XGBoost: A Scalable Tree Boosting System, in: Proceedings of the 22nd ACM SIGKDD International Conference on Knowledge Discovery and Data Mining, 785–794, <https://doi.org/10.1145/2939672.2939785>, 2016.
- Cocco, V., Joos, F., Steinacher, M., Frölicher, T. L., Bopp, L., Dunne, J., Gehlen, M., Heinze, C., Orr, J., Oschlies, A., Schneider, B., Segschneider, J., and Tjiputra, J.: Oxygen and indicators of stress for marine life in multi-model global warming projections, *Biogeosciences*, 10, 1849–1868, <https://doi.org/10.5194/bg-10-1849-2013>, 2013.
- Deutsch, C., Brix, H., Ito, T., Frenzel, H., and Thompson, L.: Climate-Forced Variability of Ocean Hypoxia, *Science*, 333, 336–339, <https://doi.org/10.1126/science.1202422>, 2011.
- Dietterich, T. G.: Ensemble Methods in Machine Learning, in: *Multiple Classifier Systems*, vol. 1857, Springer Berlin Heidelberg, Berlin, Heidelberg, 15 pp., [https://doi.org/10.1007/3-540-45014-9\\_1](https://doi.org/10.1007/3-540-45014-9_1), 2000.
- Duteil, O., Frenger, I., and Getzlaff, J.: The riddle of eastern tropical Pacific Ocean oxygen levels: the role of the supply by intermediate-depth waters, *Ocean Sci.*, 17, 1489–1507, <https://doi.org/10.5194/os-17-1489-2021>, 2021.
- Espinoza-Morriberón, D., Echevin, V., Colas, F., Tam, J., Gutierrez, D., Graco, M., Ledesma, J., and Quispe-Calluari, C.: Oxygen Variability During ENSO in the Tropical South Eastern Pacific, *Front. Mar. Sci.*, 5, 526, <https://doi.org/10.3389/fmars.2018.00526>, 2019.
- Frajka-Williams, E., Rhines, P. B., and Eriksen, C. C.: Physical controls and mesoscale variability in the Labrador Sea spring phytoplankton bloom observed by Seaglider, *Deep-Sea Res. Pt. I*, 56, 2144–2161, <https://doi.org/10.1016/j.dsr.2009.07.008>, 2009.

- Friedman, J. H.: Greedy function approximation: A gradient boosting machine, *Ann. Stat.*, 29, <https://doi.org/10.1214/aos/1013203451>, 2001.
- Gade, K.: A Non-singular Horizontal Position Representation, *J. Navigation*, 63, 395–417, <https://doi.org/10.1017/S0373463309990415>, 2010.
- Garcia, H. E., Wang, Z., Bouchard, C., Cross, S. L., Paver, C. R., Reagan, J. R., Boyer, T. P., Locarnini, R. A., Mishonov, A. V., Baranova, O. K., Seidov, D., and Dukhovskoy, D.: World Ocean Atlas 2023, Vol. 3, Dissolved Oxygen, Apparent Oxygen Utilization, and Dissolved Oxygen Saturation, NOAA Atlas NESDIS 91, NOAA, <https://doi.org/10.25923/RB67-NS53>, 2024.
- Geurts, P., Ernst, D., and Wehenkel, L.: Extremely randomized trees, *Mach. Learn.*, 63, 3–42, <https://doi.org/10.1007/s10994-006-6226-1>, 2006.
- Giglio, D., Lyubchich, V., and Mazloff, M. R.: Estimating Oxygen in the Southern Ocean Using Argo Temperature and Salinity, *J. Geophys. Res.-Oceans*, 123, 4280–4297, <https://doi.org/10.1029/2017JC013404>, 2018.
- Gouretski, V., Cheng, L., Du, J., Xing, X., Chai, F., and Tan, Z.: A consistent ocean oxygen profile dataset with new quality control and bias assessment, *Earth Syst. Sci. Data*, 16, 5503–5530, <https://doi.org/10.5194/essd-16-5503-2024>, 2024.
- Gruber, N.: The Dynamics of the Marine Nitrogen Cycle and its Influence on Atmospheric CO<sub>2</sub> Variations, in: *The Ocean Carbon Cycle and Climate*, edited by: Follows, M. and Oguz, T., Springer Netherlands, Dordrecht, 97–148, [https://doi.org/10.1007/978-1-4020-2087-2\\_4](https://doi.org/10.1007/978-1-4020-2087-2_4), 2004.
- Gruber, N.: Warming up, turning sour, losing breath: ocean biogeochemistry under global change, *Philos. T. R. Soc. A.*, 369, 1980–1996, <https://doi.org/10.1098/rsta.2011.0003>, 2011.
- Guryanov, A.: Histogram-Based Algorithm for Building Gradient Boosting Ensembles of Piecewise Linear Decision Trees, in: *Analysis of Images, Social Networks and Texts*, vol. 11832, edited by: Van Der Aalst, W. M. P., Batagelj, V., Ignatov, D. I., Khachay, M., Kuskova, V., Kutuzov, A., Kuznetsov, S. O., Lomazova, I. A., Loukachevitch, N., Napoli, A., Pardalos, P. M., Pelillo, M., Savchenko, A. V., and Tutubalina, E., Springer International Publishing, Cham, 39–50, [https://doi.org/10.1007/978-3-030-37334-4\\_4](https://doi.org/10.1007/978-3-030-37334-4_4), 2019.
- Han, M. and Zhou, Y.: Global Monthly Dissolved Oxygen Reconstruction via Bayesian Ensemble Machine Learning, Zenodo [data set], <https://doi.org/10.5281/zenodo.19705526>, 2026.
- Helm, K. P., Bindoff, N. L., and Church, J. A.: Observed decreases in oxygen content of the global ocean, *Geophys. Res. Lett.*, 38, <https://doi.org/10.1029/2011GL049513>, 2011.
- Huang, S., Shao, J., Chen, Y., Qi, J., Wu, S., Zhang, F., He, X., and Du, Z.: Reconstruction of dissolved oxygen in the Indian Ocean from 1980 to 2019 based on machine learning techniques, *Front. Mar. Sci.*, 10, 1291232, <https://doi.org/10.3389/fmars.2023.1291232>, 2023.
- Iida, T., Odate, T., and Fukuchi, M.: Long-Term Trends of Nutrients and Apparent Oxygen Utilization South of the Polar Front in Southern Ocean Intermediate Water from 1965 to 2008, *PLoS ONE*, 8, e171766, <https://doi.org/10.1371/journal.pone.0071766>, 2013.
- Ito, T., Cervania, A., Cross, K., Ainchwar, S., and Delawalla, S.: Mapping Dissolved Oxygen Concentrations by Combining Shipboard and Argo Observations Using Machine Learning Algorithms, *J. Geophys. Res.: Machine Learning and Computation*, 1, e2024JH000272, <https://doi.org/10.1029/2024JH000272>, 2024.
- Jain, V., Shankar, D., Vinayachandran, P. N., Kankonkar, A., Chatterjee, A., Amol, P., Almeida, A. M., Michael, G. S., Mukherjee, A., Chatterjee, M., Fernandes, R., Luis, R., Kamble, A., Hegde, A. K., Chatterjee, S., Das, U., and Neema, C. P.: Evidence for the existence of Persian Gulf Water and Red Sea Water in the Bay of Bengal, *Clim. Dynam.*, 48, 3207–3226, <https://doi.org/10.1007/s00382-016-3259-4>, 2017.
- Karstensen, J., Stramma, L., and Visbeck, M.: Oxygen minimum zones in the eastern tropical Atlantic and Pacific oceans, *Prog. Oceanogr.*, 77, 331–350, <https://doi.org/10.1016/j.pocean.2007.05.009>, 2008.
- Ke, G., Meng, Q., Finley, T., Wang, T., Chen, W., Ma, W., Ye, Q., and Liu, T.-Y.: LightGBM: A Highly Efficient Gradient Boosting Decision Tree, *Adv. Neur. In.*, 30, 3149–3157, 2017.
- Keeling, R. F., Körtzinger, A., and Gruber, N.: Ocean Deoxygenation in a Warming World, *Annu. Rev. Mar. Sci.*, 2, 199–229, <https://doi.org/10.1146/annurev.marine.010908.163855>, 2010.
- Kleiber, W., Raftery, A. E., Baars, J., Gneiting, T., Mass, C. F., and Gritti, E.: Locally Calibrated Probabilistic Temperature Forecasting Using Geostatistical Model Averaging and Local Bayesian Model Averaging, *Mon. Weather Rev.*, 139, 2630–2649, <https://doi.org/10.1175/2010MWR3511.1>, 2011.
- Kolber, Z. S., Van Dover, C. L., Niederman, R. A., and Falkowski, P. G.: Bacterial photosynthesis in surface waters of the open ocean, *Nature*, 407, 177–179, <https://doi.org/10.1038/35025044>, 2000.
- Kwiatkowski, L., Torres, O., Bopp, L., Aumont, O., Chamberlain, M., Christian, J. R., Dunne, J. P., Gehlen, M., Ilyina, T., John, J. G., Lenton, A., Li, H., Lovenduski, N. S., Orr, J. C., Palmieri, J., Santana-Falcón, Y., Schwinger, J., Séférian, R., Stock, C. A., Tagliabue, A., Takano, Y., Tjiputra, J., Toyama, K., Tsujino, H., Watanabe, M., Yamamoto, A., Yool, A., and Ziehn, T.: Twenty-first century ocean warming, acidification, deoxygenation, and upper-ocean nutrient and primary production decline from CMIP6 model projections, *Biogeosciences*, 17, 3439–3470, <https://doi.org/10.5194/bg-17-3439-2020>, 2020.
- Long, M. C., Deutsch, C., and Ito, T.: Finding forced trends in oceanic oxygen, *Global Biogeochem. Cy.*, 30, 381–397, <https://doi.org/10.1002/2015GB005310>, 2016.
- Mao, Z., Mao, Z., Jamet, C., Linderman, M., Wang, Y., and Chen, X.: Seasonal Cycles of Phytoplankton Expressed by Sine Equations Using the Daily Climatology from Satellite-Retrieved Chlorophyll-a Concentration (1997–2019) Over Global Ocean, *Remote Sens.*, 12, 2662, <https://doi.org/10.3390/rs12162662>, 2020.
- Matear, R. J. and Hirst, A. C.: Long-term changes in dissolved oxygen concentrations in the ocean caused by protracted global warming, *Global Biogeochem. Cy.*, 17, 2002GB001997, <https://doi.org/10.1029/2002GB001997>, 2003.
- Mishonov, A. V., Boyer, T. P., Baranova, O. K., Bouchard, C. N., Cross, S. L., Garcia, H. E., Locarnini, R. A., Paver, C. R., Reagan, J. R., Wang, Z., Seidov, D., Grodsky, A. I., and Beauchamp, J. G.: World Ocean Database 2023, NOAA Atlas NESDIS 97, NOAA, <https://doi.org/10.25923/z885-h264>, 2024.
- Morrison, A. K., Waugh, D. W., Hogg, A. McC., Jones, D. C., and Abernathy, R. P.: Ventilation of the Southern Ocean Pycnocline, *Annu. Rev. Mar. Sci.*, 14, 405–430, <https://doi.org/10.1146/annurev-marine-010419-011012>, 2022.

- Naqvi, S. W. A., Naik, H., Pratihary, A., D'Souza, W., Narvekar, P. V., Jayakumar, D. A., Devol, A. H., Yoshinari, T., and Saino, T.: Coastal versus open-ocean denitrification in the Arabian Sea, *Biogeosciences*, 3, 621–633, <https://doi.org/10.5194/bg-3-621-2006>, 2006.
- Narvekar, J., Kesserkar, P., Sreejith, K. S., Fernandes, L., and Prasanna Kumar, S.: Recent oxygenation of oxygen minimum zone in the Arabian Sea and possible causes, *Prog. Oceanogr.*, 240, 103600, <https://doi.org/10.1016/j.pocean.2025.103600>, 2025.
- Nayak, A. A., Vinayachandran, P. N., and George, J. V.: Arabian Sea high salinity core supplies oxygen to the Bay of Bengal, *Deep-Sea Res. Pt. II*, 221, 105477, <https://doi.org/10.1016/j.dsr2.2025.105477>, 2025.
- Olsen, A., Key, R. M., van Heuven, S., Lauvset, S. K., Velo, A., Lin, X., Schirnick, C., Kozyr, A., Tanhua, T., Hoppema, M., Jutterström, S., Steinfeldt, R., Jeansson, E., Ishii, M., Pérez, F. F., and Suzuki, T.: The Global Ocean Data Analysis Project version 2 (GLODAPv2) – an internally consistent data product for the world ocean, *Earth Syst. Sci. Data*, 8, 297–323, <https://doi.org/10.5194/essd-8-297-2016>, 2016.
- Oschlies, A., Brandt, P., Stramma, L., and Schmidtko, S.: Drivers and mechanisms of ocean deoxygenation, *Nat. Geosci.*, 11, 467–473, <https://doi.org/10.1038/s41561-018-0152-2>, 2018.
- Pathak, R., Dasari, H. P., Ashok, K., and Hoteit, I.: Effects of multi-observations uncertainty and models similarity on climate change projections, *npj Clim. Atmos. Sci.*, 6, 144, <https://doi.org/10.1038/s41612-023-00473-5>, 2023.
- Paulmier, A. and Ruiz-Pino, D.: Oxygen minimum zones (OMZs) in the modern ocean, *Prog. Oceanogr.*, 80, 113–128, <https://doi.org/10.1016/j.pocean.2008.08.001>, 2009.
- Prokhorenkova, L., Gusev, G., Vorobev, A., Dorogush, A. V., and Gulin, A.: CatBoost: unbiased boosting with categorical features, *Adv. Neur. In.*, 31, 6639–6649, 2018.
- Raftery, A. E., Gneiting, T., Balabdaoui, F., and Polakowski, M.: Using Bayesian Model Averaging to Calibrate Forecast Ensembles, *Mon. Weather Rev.*, 133, 1155–1174, <https://doi.org/10.1175/MWR2906.1>, 2005.
- Reichstein, M., Camps-Valls, G., Stevens, B., Jung, M., Denzler, J., Carvalhais, N., and Prabhat: Deep learning and process understanding for data-driven Earth system science, *Nature*, 566, 195–204, <https://doi.org/10.1038/s41586-019-0912-1>, 2019.
- Rippeth, T., Shen, S., Lincoln, B., Scannell, B., Meng, X., Hopkins, J., and Sharples, J.: The deepwater oxygen deficit in stratified shallow seas is mediated by diapycnal mixing, *Nat. Commun.*, 15, 3136, <https://doi.org/10.1038/s41467-024-47548-2>, 2024.
- Roach, C. J. and Bindoff, N. L.: Developing a New Oxygen Atlas of the World's Oceans Using Data Interpolating Variational Analysis, *J. Atmos. Ocean. Tech.*, 40, 1475–1491, <https://doi.org/10.1175/JTECH-D-23-0007.1>, 2023.
- Roberts, D. R., Bahn, V., Ciuti, S., Boyce, M. S., Elith, J., Guillerá-Arroita, G., Hauenstein, S., Lahoz-Monfort, J. J., Schröder, B., Thuiller, W., Warton, D. I., Wintle, B. A., Hartig, F., and Dormann, C. F.: Cross-validation strategies for data with temporal, spatial, hierarchical, or phylogenetic structure, *Ecography*, 40, 913–929, <https://doi.org/10.1111/ecog.02881>, 2017.
- Roch, M., Brandt, P., and Schmidtko, S.: Recent large-scale mixed layer and vertical stratification maxima changes, *Front. Mar. Sci.*, 10, 1277316, <https://doi.org/10.3389/fmars.2023.1277316>, 2023.
- Ryther, J. H.: Photosynthesis in the Ocean as a Function of Light Intensity<sup>1</sup>, *Limnol. Oceanogr.*, 1, 61–70, <https://doi.org/10.4319/lo.1956.1.1.0061>, 1956.
- Sampaio, E., Santos, C., Rosa, I. C., Ferreira, V., Pörtner, H.-O., Duarte, C. M., Levin, L. A., and Rosa, R.: Impacts of hypoxic events surpass those of future ocean warming and acidification, *Nat. Ecol. Evol.*, 5, 311–321, <https://doi.org/10.1038/s41559-020-01370-3>, 2021.
- Sarma, V. V. S. S. and Udaya Bhaskar, T. V. S.: Ventilation of Oxygen to Oxygen Minimum Zone Due to Anticyclonic Eddies in the Bay of Bengal, *J. Geophys. Res.-Biogeo.*, 123, 2145–2153, <https://doi.org/10.1029/2018JG004447>, 2018.
- Schmidtko, S., Stramma, L., and Visbeck, M.: Decline in global oceanic oxygen content during the past five decades, *Nature*, 542, 335–339, <https://doi.org/10.1038/nature21399>, 2017.
- Shao, J., Huang, S., Chen, Y., Qi, J., Wang, Y., Wu, S., Liu, R., and Du, Z.: Satellite-Based Global Sea Surface Oxygen Mapping and Interpretation with Spatiotemporal Machine Learning, *Environ. Sci. Technol.*, 58, 498–509, <https://doi.org/10.1021/acs.est.3c08833>, 2023.
- Sharp, J. D., Fassbender, A. J., Carter, B. R., Johnson, G. C., Schultz, C., and Dunne, J. P.: GOBAI-O2: temporally and spatially resolved fields of ocean interior dissolved oxygen over nearly 2 decades, *Earth Syst. Sci. Data*, 15, 4481–4518, <https://doi.org/10.5194/essd-15-4481-2023>, 2023.
- Shen, C.: A Transdisciplinary Review of Deep Learning Research and Its Relevance for Water Resources Scientists, *Water Resour. Res.*, 54, 8558–8593, <https://doi.org/10.1029/2018WR022643>, 2018.
- Solomon, A., Heuzé, C., Rabe, B., Bacon, S., Bertino, L., Heimbach, P., Inoue, J., Iovino, D., Mottram, R., Zhang, X., Aksenov, Y., McAdam, R., Nguyen, A., Raj, R. P., and Tang, H.: Freshwater in the Arctic Ocean 2010–2019, *Ocean Sci.*, 17, 1081–1102, <https://doi.org/10.5194/os-17-1081-2021>, 2021.
- Stramma, L., Johnson, G. C., Sprintall, J., and Mohrholz, V.: Expanding Oxygen-Minimum Zones in the Tropical Oceans, *Science*, 320, 655–658, <https://doi.org/10.1126/science.1153847>, 2008.
- Stramma, L., Schmidtko, S., Levin, L. A., and Johnson, G. C.: Ocean oxygen minima expansions and their biological impacts, *Deep-Sea Res. Pt. I*, 57, 587–595, <https://doi.org/10.1016/j.dsr.2010.01.005>, 2010.
- Stramma, L., Prince, E. D., Schmidtko, S., Luo, J., Hoolihan, J. P., Visbeck, M., Wallace, D. W. R., Brandt, P., and Körtzinger, A.: Expansion of oxygen minimum zones may reduce available habitat for tropical pelagic fishes, *Nat. Clim. Change*, 2, 33–37, <https://doi.org/10.1038/nclimate1304>, 2012.
- Talley, L.: Closure of the Global Overturning Circulation Through the Indian, Pacific, and Southern Oceans: Schematics and Transports, *Oceanography*, 26, 80–97, <https://doi.org/10.5670/oceanog.2013.07>, 2013.
- Tang, W., Li, Z., and Cassar, N.: Machine Learning Estimates of Global Marine Nitrogen Fixation, *J. Geophys. Res.-Biogeo.*, 124, 717–730, <https://doi.org/10.1029/2018JG004828>, 2019.

- Wang, Z., Garcia, H. E., Boyer, T. P., Reagan, J. R., Maurer, T., Ito, T., Sharp, J. D., Cross, S., and Bouchard, C.: Bias Evaluation for Sensor-Based Dissolved Oxygen from CTD and Profiling Floats in the World Ocean Database, *J. Atmos. Ocean. Tech.*, 42, 1263–1280, <https://doi.org/10.1175/JTECH-D-25-0027.1>, 2025.
- Wong, A. P. S., Wijffels, S. E., Riser, S. C., Pouliquen, S., Hosoda, S., Roemmich, D., Gilson, J., Johnson, G. C., Martini, K., Murphy, D. J., Scanderbeg, M., Bhaskar, T. V. S. U., Buck, J. J. H., Merceur, F., Carval, T., Maze, G., Cabanes, C., André, X., Poffa, N., Yashayaev, I., Barker, P. M., Guinehut, S., Belbéoch, M., Ignaszewski, M., Baringer, M. O., Schmid, C., Lyman, J. M., McTaggart, K. E., Purkey, S. G., Zilberman, N., Alkire, M. B., Swift, D., Owens, W. B., Jayne, S. R., Hersh, C., Robbins, P., West-Mack, D., Bahr, F., Yoshida, S., Sutton, P. J. H., Cancouët, R., Coatanoan, C., Dobbler, D., Juan, A. G., Gourrion, J., Kolodziejczyk, N., Bernard, V., Bourlès, B., Claustre, H., D’Ortenzio, F., Le Reste, S., Le Traon, P.-Y., Rannou, J.-P., Saout-Grit, C., Speich, S., Thierry, V., Verbrugge, N., Angel-Benavides, I. M., Klein, B., Notarstefano, G., Poulain, P.-M., Vélez-Belchí, P., Suga, T., Ando, K., Iwasaka, N., Kobayashi, T., Masuda, S., Oka, E., Sato, K., Nakamura, T., Sato, K., Takatsuki, Y., Yoshida, T., Cowley, R., Lovell, J. L., Oke, P. R., Van Wijk, E. M., Carse, F., Donnelly, M., Gould, W. J., Gowers, K., King, B. A., Loch, S. G., Mowat, M., Turton, J., Rama Rao, E. P., Ravichandran, M., Freeland, H. J., Gaboury, I., Gilbert, D., Greenan, B. J. W., Ouellet, M., Ross, T., Tran, A., Dong, M., Liu, Z., Xu, J., Kang, K., Jo, H., Kim, S., and Park, H.: Argo Data 1999–2019: Two Million Temperature-Salinity Profiles and Subsurface Velocity Observations From a Global Array of Profiling Floats, *Front. Mar. Sci.*, 7, 700, <https://doi.org/10.3389/fmars.2020.00700>, 2020.
- Wu, Y., Zheng, Z., Chen, X., Zhong, W., Yuan, X., Zhong, W., Lei, R., Li, C., Zhuang, Y., Gao, X., Li, X., Lin, H., Chen, L., Cai, W.-J., and Qi, D.: Amplified warming accelerates deoxygenation in the Arctic Ocean, *Nat. Clim. Change*, 15, 859–865, <https://doi.org/10.1038/s41558-025-02376-0>, 2025.
- Zhang, Z., Ma, W., and Chai, F.: Role of ocean circulation and settling of particulate organic matter in the decoupling between the oxygen minimum zone and the phytoplankton productive zone in the Arabian Sea: A modeling study, *Front. Mar. Sci.*, 9, 927921, <https://doi.org/10.3389/fmars.2022.927921>, 2022.
- Zhou, Y., Gong, H., and Zhou, F.: Responses of Horizontally Expanding Oceanic Oxygen Minimum Zones to Climate Change Based on Observations, *Geophys. Res. Lett.*, 49, e2022GL097724, <https://doi.org/10.1029/2022GL097724>, 2022.